THE EVALUATION OF PERMEABLE LOW-DENSITY CELLULAR CONCRETE AS A POTENTIAL SUBBASE MATERIAL IN ROADWAY SYSTEMS

by

Tatiana de Camargo Gontscharow

A thesis submitted to the faculty of
The University of Utah
in partial fulfillment of the requirements for the degree of

Master of Science

Department of Civil and Environmental Engineering

The University of Utah

August 2023

The University of Utah Graduate School

STATEMENT OF THESIS APPROVAL

The thesis of **Tatiana de Camargo Gontscharow**

has been approved by the following supervisory committee members:

Steven F. Bartlett	, Chair	**07/12/2023** Date Approved
Emily Marron	, Member	**07/10/2023** Date Approved
Shahrzad Roshankhah	, Member	**07/10/2023** Date Approved

and by **Michael Ernest Barber** , Chair/Dean of

the Department/College/School of **Civil and Environmental Engineering**

and by Darryl P. Butt, Dean of The Graduate School.

ABSTRACT

This paper discusses the mechanical characteristics of Permeable Low-Density Cellular Concrete (PLDCC) and its capacity to support pavement systems as a subbase material. PLDCC has a relatively high permeability coefficient similar to clean, coarse sand and a water storage capacity of up to 60% by volume. However, the potential use of PLDCC as subterraneous detention/retention basins for decentralized stormwater management systems (DSWMS) and for roadway, building, and retaining wall drains and water filters is developing. Also, the increasing potential for urban flooding, aggravated by global warming and urban hardscape, gives impetus to develop these applications. One uncertainty not addressed for roadway systems is PLDCC's structural response in pavement systems as a subbase or base material. Specifically, pavement design inputs (e.g., Resilient Modulus) are missing from the engineering literature. We subjected PLDCC samples low-strain cyclic axle loads to obtain their Resilient Modulus (RM) values. Those samples were subsequently tested in uniaxial compression, and the unconfined compression (UC) results were compared with the corresponding RM values. This comparison indicates that RM values are acceptable for use as a pavement subbase. In addition, the results were used to evaluate how substituting a regular granular subbase material with PLDCC could affect long-term pavement performance. This evaluation utilized the Guide for Mechanistic-Empirical Design of Pavement Structures approach. Our research suggests PLDCC's mechanical properties make it a viable alternative to

granular subbases for traditional pavement systems. However, we did not evaluate the effect of the degree of saturation on the mechanical properties of PLDCC and recommend this topic for future research.

TABLE OF CONTENTS

LIST OF TABLES

Tables

ACKNOWLEDGMENTS

I want to thank Dr. Steven Bartlett for his guidance in this project and mentorship throughout the graduation process. I also thank and recognize the funding support of the National Center for Transportation Infrastructure Durability and Life-Extension (TriDurLE) and the University of Utah. AERIX Industries, the University of Utah Asian Campus (UAC), and IGES Inc. provided in-kind matching contributions, project technical support, and advice. In addition, I thank Dr. Emily Marron, Dr. Shahrzad Roshanlhah, and the Thesis Office team for reviewing this paper. And finally, I would like to express my gratitude to Yaqi Huang, Christopher Anderson, the Nair family, the Buchman family, and my family for their support over the years.

CHAPTER 1

INTRODUCTION

The widespread impermeabilization of the soil is the most prevalent form of deterioration of urban soil because of its damaging results on the soil hydrology, the thermal capacity, and its consequences over biochemical cycles [1]. Even the impermeabilization of small isolated areas such as residential gardens also had been related to the potential frequency and severity intensification of urban flooding by studies conducted over decades in the United Kingdom [2]. In addition, about a quarter of the impermeabilization in a metropolitan area is given to the presence of road surfaces [3].

Permeable pavements have the potential to be a critical addition to the mitigation of issues related to extensive hardscaping. Thus, the improvement of this technology has been pointed out as essential for developing runoff auto-regulated urban areas, also named Sponge Cities, which can be understood as a DSWMS (decentralized stormwater management system). This urban model was first presented in China in 2012 [4], and since then, it has obtained considerable popularity in other Asian countries such as South Korea.

Permeable pavements typically comprise a top layer of Permeable Concrete, pavers, or porous asphalt, followed by a coarse aggregate layer (base) and subgrade soil [5]. Also, adding a second base, the subbase layer, is a standard procedure to reduce the

stress over the subgrade [6]. The base and subbase layers of permeable pavements, which have considerable influence over the response of the pavement to traffic loads [7] and offer structural support for this structure, are vital for the design of the volume of water accepted by permeable pavement systems [3].

Considering the importance of such layers in the system for the actual volume of water retained and the reduced life span of permeable pavements due to the fast deterioration of their top layers, new models of “semi-permeable” pavements have been developed. An example is the plan to install regular surface pavement layers over permeable subbases connected to lateral channels, allowing the runoff to access the coating designed to operate as an urban reservoir, at Sejong City in South Korea.

However, as Shackel [3] points out, permeable bases and subbases are currently composed of the same granular materials used at such layers of conventional pavements. In addition, the design of such unbound layers is made using the same procedure independently of the permeability aimed for the pavement system. Thus, Shackel [3] draws attention to the necessity of developing materials and techniques that improve the permeability and resistance of the so-called granular, or coarse, layers of the permeable pavements.

This way, it is believed that such coarse layers can be substituted by a Permeable Low-Density Cellular Concrete (PLDCC) layer. The PLDCC can reach a relatively proper compressive strength of about 160 psi (1.1 MPa) while keeping an excavatable feature. In addition, this material also presents high permeability with a coefficient of permeability ranging between 0.001 and 1 cm/sec, comparable to coarse, clean sand and

gravel mixtures. It is also pointed out that this material maintains its compressive strength at oscillating saturation levels and can be easily placed in the field [8].

Contemporary PLDCC has been used in many geotechnical-related applications, such as pavement subbase layers [9]. However, the response of this material to traffic loads is still unknown. The current literature about this material over this scenario strongly focuses on its high permeability, lightweight characteristics, and possible clogging problems. Thus, the reaction of the PLDCC to traffic loads is addressed in this study.

CHAPTER 2

LITERATURE REVIEW

Low-Impact Development Approaches and the Development of Permeable Pavements

Besides the lack of accurate data on flooding in the United States, it is estimated that each county had losses of $200 million per year from 2004 to 2014. However, the actual amount of losses is much higher since historical estimates, like this one, ignore pluvial flooding, uninsured property losses, indirect losses, and other essential factors. In addition, flooding is considered a natural hazard with higher social and economic impacts on the American population [10]. The same situation is observed on a global scale.

This worldwide flooding scenario will increase in the following years due to the consequences of global warming, which will trigger an increased frequency of sudden heavy rain events. Such events are 7% more probable for each degree augmented in the overall planet's temperature [11]. Furthermore, these rains are not only happening with a higher frequency but also with a higher intensity, which frequently contributes to water quality decline. This trend has been reported in South America since the early 20th century and in North America since the mid-20th century [11]. Revising this trend is one of the biggest challenges for the continued development of many Asian countries.

Countries like China and South Korea have experienced fast urban development over the past decades, reflected in the rampant installation of hardscaping or impervious surfaces. As a result of the extensive hardscaping, the urban flooding phenomenon intensified even more. For example, in Hohhot, a city in China, the increase in impervious surfaces contributes two to four times more to the flooding risk than the action of climate change. In addition, the current flood protection infrastructure in South Korea is expected to comport only about 30% of future flood levels by 2100 [11].

Thus, it is unsurprising that the reduction in flooding risks with land planning systems has been intensely discussed in this region, which originated the concept of Sponge Cities [12]. This concept was first proposed in China in 2012 and can be defined as low-impact construction concentrated on runoff management, augmenting the resilience of urban environments concerning water-related challenges [4, 13, 14]. For that, the development of a sponge city is based on four main principles: to safeguard urban water resources, to promote ecological water management, to promote the installation of green infrastructure, and to install permeable pavement [15].

The differentiation of the permeable pavements from other green infrastructure, such as green roofs, reinforces this element's importance in urban centers. It is estimated that between 20 and 25% of the impervious surface of a city is composed of roads [16]. Moreover, substituting these traditional pavements for permeable ones, with graded gravel layers as thin as 36.4 cm, can promote a runoff volume reduction of almost 75% with a pollutant removal effectiveness reaching 99% [17]. Other than the positive results over rainwater quality and management, permeable pavements can also be related to

noise reduction, increased skid resistance [18], and a reduction of the Urban Heat Island effect [4].

A pavement's primary function is distributing the tire loads acting on it, thus providing a durable and functional surface for vehicles. This pavement system usually comprises the following sublayers placed atop the subgrade: subbase, base, and pavement surface (usually concrete or asphalt). Furthermore, the material's strength and durability are generally higher for the top layers, offering surface runoff drainage for the pavement to promote a safer and longer roadway life span [19]. Moreover, permeable pavements, which are consisted of layers and have been used since the 18th century to handle water runoff, function as a water system and a load-bearing structure [20]. Thus, the permeable pavement must be engineered considering hydrological, and structural analyses, in addition to the depth and performance of the underlying layers [21].

Permeable pavement systems can be designed as full, partial, or no infiltration systems, referring to the amount of water the subgrade will receive [20]. For example, all the layers are porous on a fully permeable pavement. The pavement acts as a reservoir that allows the stormwater to infiltrate slowly into the subsoil while avoiding spillovers [22], which could originate floods. In the other two designs, the permeable pavement works as a reservoir connected with a regular drainage system that captures the stormwater partially or totally [20].

The layers of permeable pavement are composed of a permeable surface, followed by coarse-soil-like or granular materials layers over the subsoil [5, 6]. This permeable surface can comprise permeable concrete or asphalt, interlocking pavers (made of permeable materials or not), or grid systems [1, 5, 20]. Furthermore, adding geo-textiles

between the permeable pavement layers is not unusual, especially to separate the granular layers from the surface layer to minimize clogging issues. Adding geotextiles can also reduce pollutants in the runoff while usually reducing the overall pavement permeability [5, 21].

Once the rainwater passes the surface layer, the amount of additional water absorbed by the system depends on the permeability and depth of the granular layers [3], which are the base and the subbase that effectively function as a reservoir. Shackel (2006) also points out that permeable eco-pavement base and subbase should be able to remove contaminants from the runoff while satisfying geotechnical filter criteria - which avoids the movement of fine particles between the different layers, besides offering adequate stiffness and water storage capacity.

In addition, these layers are usually constituted by the same material utilized on conventional pavements [3], such as crushed rock, which has a maximum amount of 40% of its volume composed of voids that can be occupied by water [9]. The design of permeable bases and subbases are typically made through the Moulton (1979) or the Casagrande and Shannon (1952) method. The Moulton method is based on the concept that the layer's thickness must be equal to or greater than the flow depth, while the Casagrande and Shannon method is based on studies related to freeze-thaw-susceptible and considers the time to drain [19].

Lastly, there appears to be a need for new materials with high permeability and good structural properties to substitute the granular materials currently used in the lower layers of permeable pavements [3] that are now restricted to parking lots and commercial areas with light traffic loads and low speeds [21].

Low-Density Cellular Concrete Technology

Low-density cellular concrete (LDCC) has two main characteristics: its small weight, in relationship with regular concrete, and the presence of cavities like bubbles in its composition, which make it reasonably easy to be identified. However, there is evidence of the Romans' production of materials with similar characteristics, which were probably obtained by the mixture of animal blood, small coarse sand, hot lime, and water [23]. Less gruesomely, a similar material's structure was obtained and used in human-made facilities using volcanic ash as fine aggregate around 3,000 years ago [24].

Nevertheless, the history of such kind of concrete inside modern civil engineering knowledge started only in 1934 with Bayer V. Rice patenting the Lightweight Cellular Concrete (LCC) [25], a material destined to be used as an insulation product [26]. The LCC continued to be developed and analyzed over the following years; before 2000, it was already used in void fillings, ground stabilizations, and as a building material [26].

Currently, LDCC is defined as concrete with an oven-dry density of 50 lb/ft3 (800 kg/m3), made by the mix of hydraulic cement, water, and preformed foam, with or without adding aggregates and other components such as fly ash and chemical admixtures. [27]. The LCC also is commonly referred to as Foam Concrete, Controlled Low-Strength Cellular Concrete, and Low-Density Cellular Concrete (LDCC) [25].

Adding preformed foam creates the cellular structure in LDCC. However, other less efficient methods can be used to create these cavities, such as adding aerating agents. These agents produce chemical reactions during the mixing process resulting in gas production that consequently includes the air cells or the addition of pre-foaming agents in the water [26].

Nevertheless, the addition of preformed foam has been the principal means of obtaining the air cells for the LDCC structure since the introduction of synthetic-based foam liquid concentrated in the 1990s to substitute the protein-based foam liquid concentrated. This substitution resulted in higher longevity and stability of the LDCC due to the higher stability of the air bubbles inside the concrete structure [9].

The foam content has severe implications over the fresh and the hardened LDCC characteristics. For example, excess foam can cause a drop in the flow rate in the fresh state. Other than the stability of the material, the foam content also has a massive effect on the compressive strength of the hardened LDCC [23]. Synthetic foaming agents are amphiprotic and hydrophilic substances that, by reducing the surface tension of dilution, create a material with lower density. Being essential to note that this foaming creates a complex chemical environment in which the compatibility of the cement and the surfactant is critical to determine the entrance of air and the development of the cellular structure [28]. The foaming agents should be tested before being used to ensure their properties. The commercially available ones must meet the requirements of ASTM C869, the Standard Specification for Foaming Agents Used in Making Preformed Foam for Cellular Concrete [25].

When fresh, the LDCC is in a liquid state, which allows it to be easily pumped and makes it a self-compacting material. This fresh state characteristic makes the LDCC have excellent workability. Moreover, this characteristic can be altered with oscillations in factors such as mix design, temperature, and agitation time [27]. The consistency of the LDCC can also be strongly altered with the use of superplasticizers and other

components, such as fly ash, which decreases the material viscosity by augmenting the presence of fines and water demand [26].

The main physical properties influencing LDCC performance are dry shrinkage, the air-void system, and water absorption [26]. As with any Portland cement product, the LDCC experiences drying shrinkage. This shrinkage can be up to ten times more intense in this material than in regular concrete due to decreased water content in the cement paste. For most LDCC designs, especially for geotechnical fill environments in which the verification of this phenom is complex, the shrinkage can be assumed as 0.5 to 1% [25]. In addition, the air-void system is strongly linked with the air-cell structure and formation, as the addition of fines and other additives to the mix [26].

Furthermore, the volume of water absorbed by the LDCC is nearly double that of regular concrete. This amount is not strongly influenced by the amount of air in the material, which suggests that some of the voids are filled with water [29]. Besides being dependent on the material age, porosity, and density, the mechanical properties of the LDCC, such as Compressive strength, tensile strength, and Modulus of elasticity, are smaller than those of regular concrete [26].

With all these points considered, the LDCC's low weight and excellent thermal properties, due to the incorporation of the air cells in the material composition, make its use advantageous in building applications. It can be easily employed in building blocks and panels, supporting considerable loads, and offers excellent results when used in roof insulation [30]. In the geotechnical field, some typical applications of the LDCC are Tunnel Backfills, and Annular Fills, Subgrades Modifications and Tremie Applications,

Bridge Approaches and Retaining Wall Backfills, Underground Utility Protection, and Fill for Underground Tanks, Pipelines, Abandoned Mines, and Conduits [9].

In the 2000s, the creation of foam based on a mix of protein and synthetic elements enabled the connection between the air cells in the LDCC, forming pores and allowing water passage through this substance. This variation was named Permeable Low-Density Cellular Concrete (PLDCC) [9]. The characteristics pores of the LDCC and the PLDCC can be observed in Figure 1.

The PLDCC has a high concentration of pores that interconnect each other, forming an intricate structure. Such structure, formally defined as a coalesced cellular structure, is responsible for the penetrability capacity of this material. Besides the high permeability, the PLDCC has the same general characteristics as the LDCC. Thus, the PLDCC is also significantly influenced by the amount and type of foaming agent used in its composition. This influence can be observed in Figure 2.

Furthermore, the PLDCC has some characteristics that make it attractive for geotechnical projects. One is the relatively proper compressive strength it can reach - about 160 psi (1.1 MPa) - while keeping an excavatable feature. The high permeability, comparable to clean sands, is another exciting feature that can be observed in Figure 3. In addition, this material maintains its compressive strength even when partially or fully saturated [8].

PLDCC has been used for several geotechnical applications. Thus, this material has been deployed for retaining wall backfills, foundation fillings, permeable and regular pavements subbases, and pool decks. PLDCC has also been used in challenging soft-soil remediation projects like the one developed at the Louis Armstrong International Airport

in New Orleans, Louisiana. In this project, it was critical to construct a vital airfield lighting vault over a black plastic clay soil base with a high-water level. Thus, the PLDCC, protected against silt infiltration with a silt fabric, assisted significantly with the runoff drainage, simultaneously offering stabilization for the soil [9].

Another example of PLDCC application as a soft-soil remediation is the reconstruction of the pavement of West Lake Eloise Drive in Winter Haven, Florida. Besides the soil stabilization, this concrete also allowed for the road's elevation augmentation. The PLDCC use in this project was remarkable due to the outstanding results. Thus, it represents an interesting study case for understanding the PLDCC potential [31].

The West Lake Eloise Drive is allocated over a soft soil area between the lakes Eloise and Lulu, being crossed daily for about 4,000 vehicles. However, even before the start of the utilization of this road, it had presented continuous settlement—resulting in costly construction and posterior maintenance. When the project team concluded that this road needed an unorthodox intervention, it was already composed of five layers of asphalt, road base, and fill soil sheets that had been added over time to deal with the settlement and flooding occurrences [31].

Eskew and Hill et al. (2021) indicate in their paper that, in this scenario, the only reasonable solution would be the remotion of all these layers and the use of lightweight fill. PLDCC was selected among all the lightweight materials in the market due to its material characteristics and cost. The main advantage of using this concrete was starting and efficiently keeping the water level equilibrium over the roadway sides. Which significantly reduced the buoyancy forces due to the reduction of the hydrostatic Pressure

and abolished the cross-drains need—reinforcing the optimal performance of the PLDCC over regions of the oscillating water table.

These projects show that the PLDCC has excellent potential in civil construction, especially in geotechnical projects in areas with high water table oscillation. This potential has increased over time due to the constant upgrading of the PLDCC's technology, allowing the production of more permeable and resistant PLDCCs with lower buoyance values. Furthermore, the future enhancement of these characteristics makes the PLDCC a strong candidate for applications in new projects where permeability and water storage are essential (e.g., improving the efficiency of permeable surfaces and subsoil reservoirs).

Additionally, it is noteworthy that neither Low-Density Cellular Concrete (LDCC) nor Permeable Low-Density Cellular Concrete (PLDCC) is expected to be exposed directly to the environment [8]. Thus, PLDCC should not be used as the wearing surface of a permeable pavement system, but it may be possible to use it as a base or subbase of such pavement.

Moreover, the lightweight feature of the PLDCC also brings concern about its use in such pavements system due to the possible creation of buoyancy forces in case of heavy sudden rain events [32]. This concern is valid since this concrete will not reach total saturation [8]. Therefore, these authors strongly suggest creating an infiltration rate of 50 to 55% into the PLDCC mix to avoid adverse events of such force.

Inti and Evans III et al. [32] investigated the results of a partial substitution of the subbase layer, originally composed solely of No. 57 aggregate, for PLDCC in a permeable pavement of a parking lot. They hypothesized that clogging would not be a

determinant factor in the used system, so they concluded that this concrete could effectively substitute partially coarse aggregate layers at the structure of permeable parking lots. Once it presents compressive strength and permeability inside the necessary range for this application, however, they point out that, in their analysis, adding this extra PLDCC layer reduced the system infiltration rate. In addition, they express the need for an analysis of the runoff properties alteration due to applying the PLDCC as the possible environmental advantages linked to this material usage.

Nonetheless, the fast development of this technology has already produced PLDCCs that present better characteristics than the ones analyzed by Inti and Evans III et al. [32] studies. More modern PLDCC, such as the one produced with the AQUAERiX-LB foaming agent, may have a more positive impact on the overall performance of the permeable pavements than the older version utilized by Inti and Evans III et al. [32]. Using PLDCC in sub-layers of a permeable pavement may also reduce the clogging of the top layers by the retention of particles that the elevation of the water table may bring, which can extend the pavement's life. A comparison between PLDCC samples made with the foaming agent AQUAERiX-LB and its ancestor can be observed in Figure 4.

Ultimately, the PLDCC's current characteristics and potential make this material have promising prospects for future applications. PLDCC can augment underlying layers' permeability and storage capacity when associated with pavement structures, thus creating a water storage reservoir for urban centers. However, further research on this material is still needed, especially concerning its mechanical properties, durability, and response to cyclic and vibratory loads.

Figure 1. Comparison between permeable and non-permeable Low-Density Cellular Concrete.

In the figure on the left, it is possible to observe the surface of a sample of Low-Density Cellular Concrete (LDCC), in which the isolation of the voids is easily identified. While in the figure on the right, the interconnection of the gaps forming the coalesced cellular structure of the Permeable Low-Density Cellular Concrete (PLDCC) is presented.

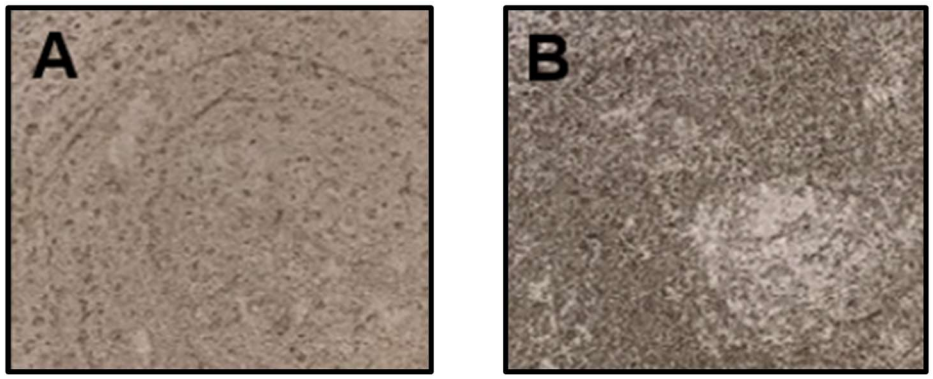

Figure 2. Comparison between Permeable Low-Density Cellular Concrete samples of different densities.

The density difference of the samples above is given solely by the different amounts of foaming agent added. Sample A, on the left, has a fresh density of approximately 30 pcf (480.55 kg/m^3), while sample B has a fresh density of 25 pcf (400.46 kg/m^3). Thus, a more significant quantity of foaming agent was added in sample B, which has consequences over the total amount of existing voids and makes the coalesced structure more visible. Therefore, sample B has a higher permeability and a lower resistance than sample A.

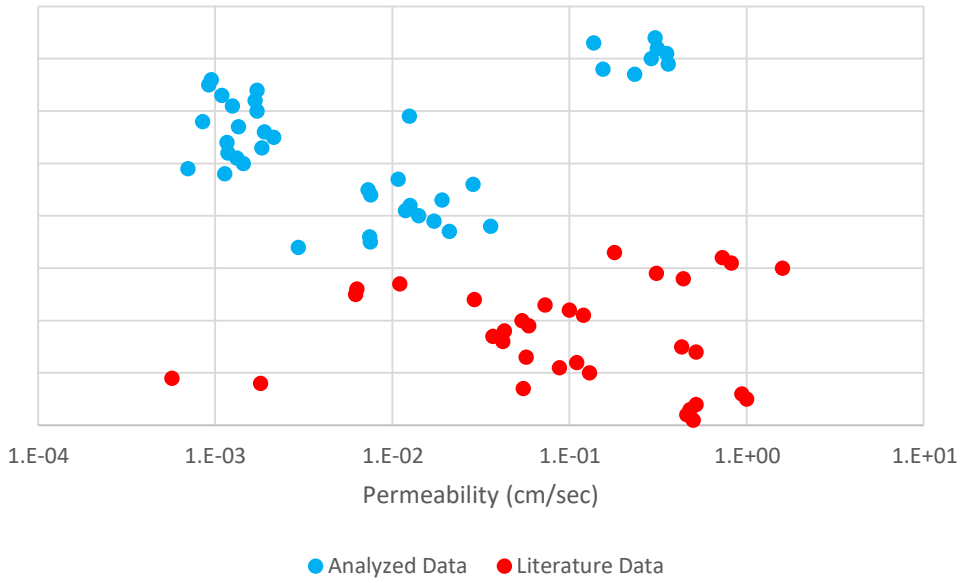

Figure 3. Permeability of different PLDCC samples.

The permeability of the eight batches of PLDCC can be observed in this figure. This material's overall range of permeability oscillated between 0.001 and 1 cm/sec, corresponding to the permeability range of sands.

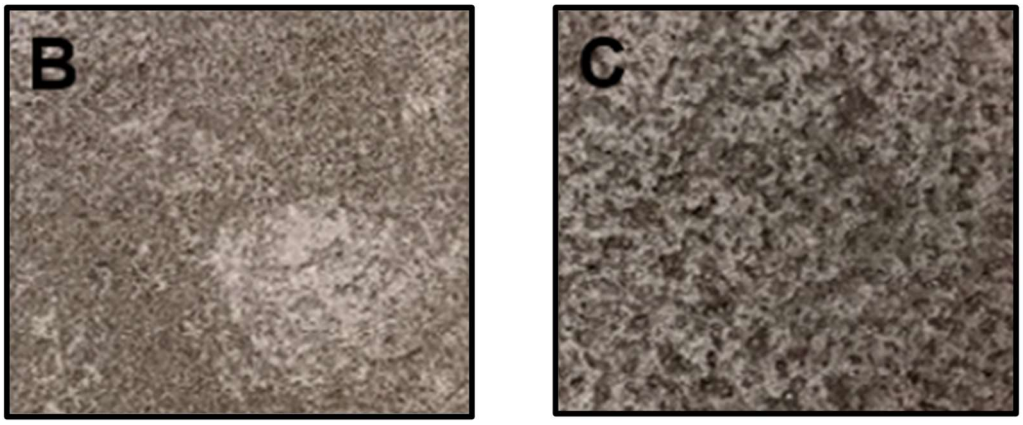

Figure 4. Comparison between Permeable Low-Density Cellular Concrete samples made with different foaming agents.

Both the samples above, B and C, have a fresh density equal to 25 pcf (400.46 kg/m^3). Sample C was produced using the foaming agent AQUAERiX-LB, while sample B was made with the antecedent of it. The higher presence of pores in C, visible in the figure, indicates a higher permeability of this sample and a higher efficiency of the AQUAERiX-LB than its predecessor.

CHAPTER 3

METHODS

As discussed in the previous chapter, PLDCC can fill the need for more resistant and permeable bases and subbases of permeable pavement systems. Those layers must meet structural and external loading demands for these systems as the project's hydrological requirements. Because permeable pavements are usually designed to provide some runoff storage, the hydrological conditions are an essential part of the design. Unfortunately, previous PLDCC research has focused on its hydrologic properties. However, research regarding its mechanical properties related to mechanistic pavement design is lacking. To fill this research gap, 12 PLDCC samples were created, and Resilient Modulus and uniaxial compressive were evaluated using the procedures below.

Samples Production

Twelve samples of PLDCC were produced in cylindrical molds of 3 in diameter by 6 in height along three batches, described in Table 1. The PLDCC utilized in this study was produced by the combination of slurry, composed of cement type I/II with water in a proportion of 1:0.55, with foam with a density of 2.5 pcf (approximately 0.393 kN/m3).

This foam was produced utilizing water, AQUAERiX-LB foaming agent, and adequate pump equipment, as shown in Figure 5. This foaming agent and the laboratory equipment to make the PLDCC used in this study were developed by AERIX Industries.

Samples Testing

These PLDCC specimens were subjected to uniaxial compression tests after it was verified that the samples did not show any detectable fractures from the Resilient Modulus testing. This latter test was used to index the specimens' quality, as routinely done in QC (quality control) testing for PLDCC and other cellular concrete products.

The Resilient Modulus is an effective way to characterize the stiffness of the various layers used in the pavement system (pavement, base, subbase, and subgrade materials). It is an essential input property to mechanistic pavement design. Subsequently,

Resilient Modulus

The Resilient Modulus is the ratio between the axial cyclic Stress and the recoverable strain. This Modulus is obtained through repeated cyclic stress-controlled triaxial tests that subject the testing samples to a fixed stress for 0.1 seconds, followed by a rest period of 0.9 seconds. During the cyclic loading, the specimens were subjected to relatively low confining pressures in the triaxial device, similar to a wide range of Pressure that might be encountered in the in-situ condition under dead and live loads (Table 2). In addition, resilient modulus testing also allows the examination of samples over different ranges of moisture content, density, and temperature [33]. However, these

variables were not explored during this study. In this study, the PLDCC samples of different densities were submitted to the resilient modulus testing using the testing sequence established by AASHTO TP46-94 in a dry state.

Uniaxial Compressive Strength

Compressive strength tests were conducted on the samples previously tested for the resilient Modulus following the ASTM C 495. In the end caps, durometers (DURO 50) were utilized. Thus, the software reports were corrected to not account for displacements referring to the durometer.

Table 1. Permeable Low-Density Cellular Concrete (PLDCC) batches data.

Batch	Production Date	Foam Density (PCF)		PLDCC Density (PCF)		
				Fresh		Dry
		Target	Actual	Target	Actual	
0	September 22, 2022	2.5	2.58	30	29.60	23.23
1	November 24, 2022	2.5	2.43	25	24.00	20.08
2	December 19, 2022	2.5	2.45	25	25.27	21.14

Table 2. Testing sequence for base/subbase materials under AASHTO TP46-94.

Sequence Number	Confining Pressure (psi)	Deviator Stress (psi)	Number of Pulses
Conditioning	15.0	15.0	500
1	3.0	3.0	100
2	3.0	6.0	100
3	3.0	9.0	100
4	5.0	5.0	100
5	5.0	10.0	100
6	5.0	15.0	100
7	10.0	10.0	100
8	10.0	20.0	100
9	10.0	30.0	100
10	15.0	10.0	100
11	15.0	15.0	100
12	15.0	30.0	100
13	20.0	15.0	100
14	20.0	20.0	100
15	20.0	40.0	100

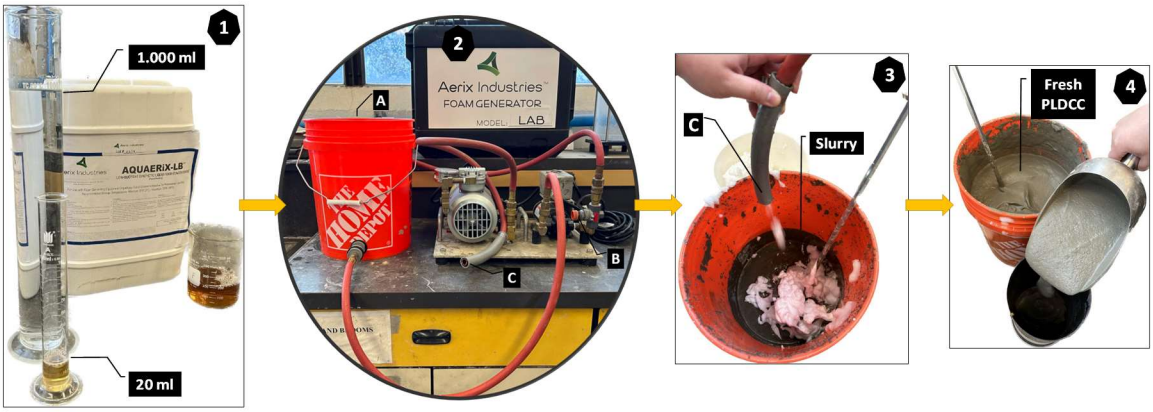

Figure 5. Laboratorial Permeable Low-Density Cellular Concrete (PLDCC) production.

On 1, it is possible to observe the appearance of the AQUAERiX-LB and the proportion of this foaming agent with water (20 ml to each 1.000 ml of water) used. This proportion was added to the A bucket that supplied the foam generator. The generator can be seen on 2, and it is vital to notice that the valve at B controls the foam density intake to the generator; and C is the foam's exit point (i.e., hose). On 3, it is possible to observe the addition of foam to the slurry that, after mixing, forms the PLDCC, which can be observed in its fresh state on 4.

CHAPTER 4

RESULTS

The resilient modulus test results and the uniaxial compressive strength test results of the twelve PLDCC samples, presented in graph format, are grouped by their respective batches in this chapter. Figures 6, 7, and 8 show the graphs obtained through the resilient modulus tests of batches 0, 1, and 2. And similarly, Figures 9 to 14 show the graphs obtained through the uniaxial compressive strength tests of batches 0, 1, and 2.

The individual results of each PLDCC sample can be seen in Appendix A, the resilient modulus test, and Appendix B, the uniaxial compressive strength tests. In Appendix C, the technique used to transform standard scale graphs to the log-log scale, used at graphs presented at Figures 6, 7, and 8, is explored.

The Resilient Modulus can be represented in terms of Bulk Stress, which is obtained by dividing the vertical force acting on the sample by its area, through the following equation:

$$MR = K_1 * \theta^{K_2} \quad \text{[Eq. 1]}$$

Where: MR = Resilient Modulus (MPa)

Θ = Bulk Stress (kPa)

K_1 and K_2 = Material's Constant (-)

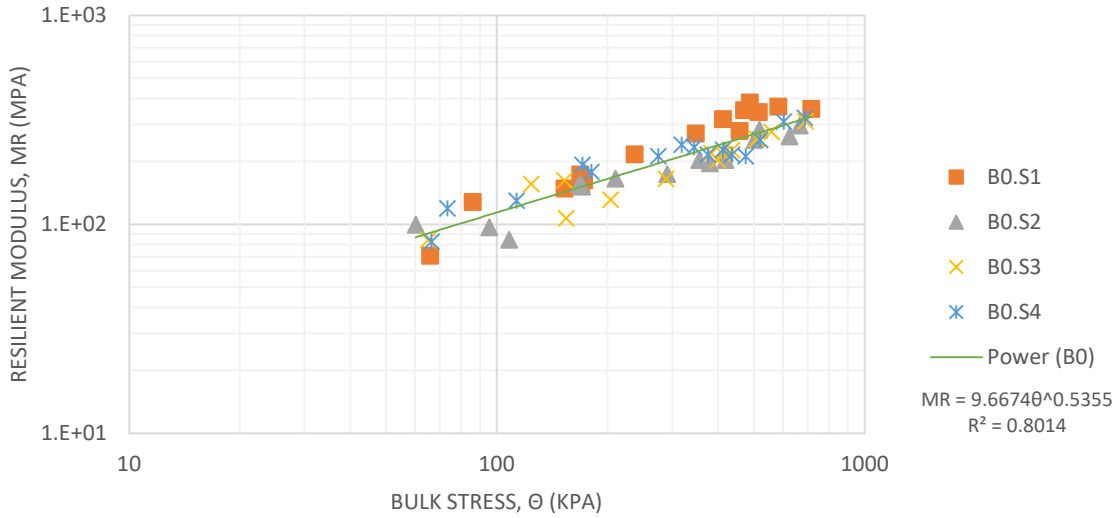

Figure 6. Graphical result of the resilient modulus test on samples of batch 0.

In this case, the material's constant K1 and K2 are equal to 9.6674 and 0.5355. The indicator R squared (R2) equals 0.8014, which suggests a relatively strong correlation.

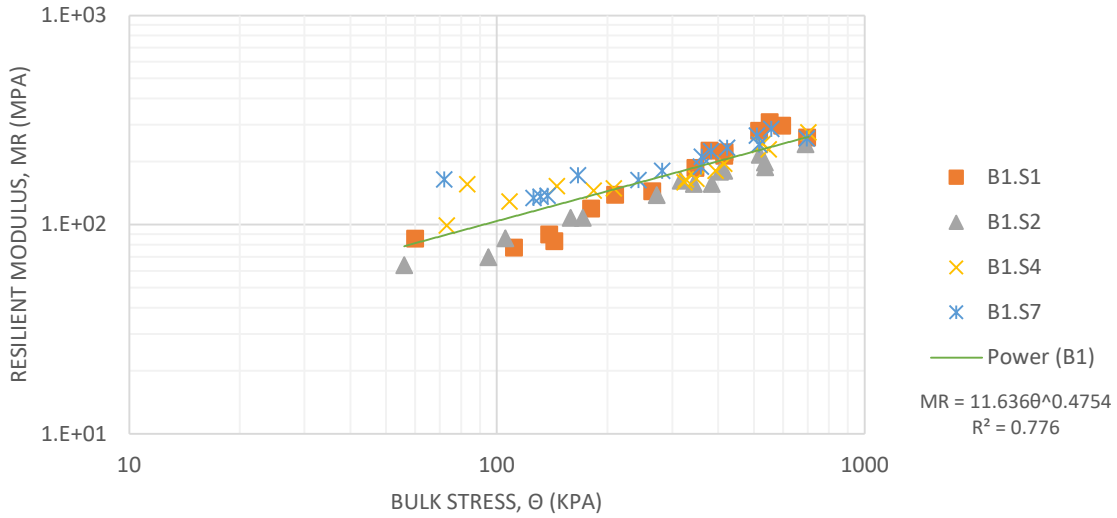

Figure 7. Graphical result of the resilient modulus test on samples of batch 1.

In this case, the material's constant K1 and K2 are equal to 11.636 and 0.4754. The indicator R squared (R2) is 0.776.

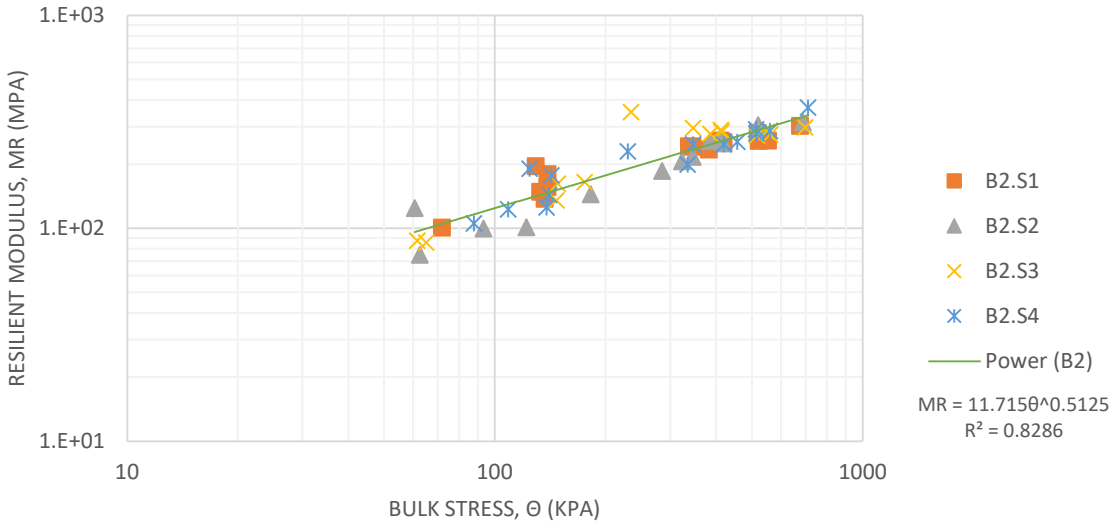

Figure 8. Graphical result of the resilient modulus test on samples of batch 2.

In this case, the material's constant K1 and K2 are equal to 11.715 and 0.5125. The indicator R squared (R2), which determines how strong is the correlation between the variables in the graph, is equal to 0.8286.

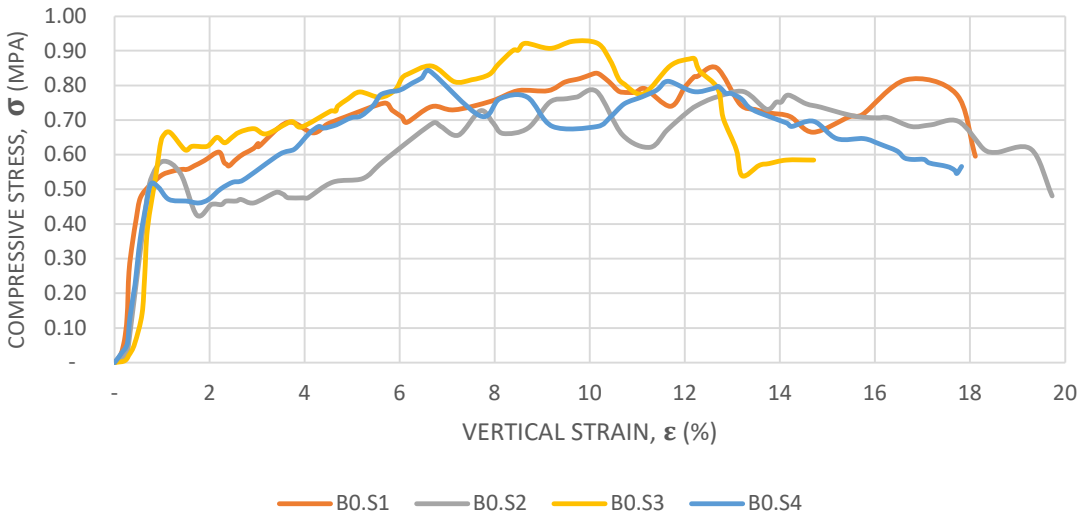

Figure 9. Unconfined compression test graph of batch 0.

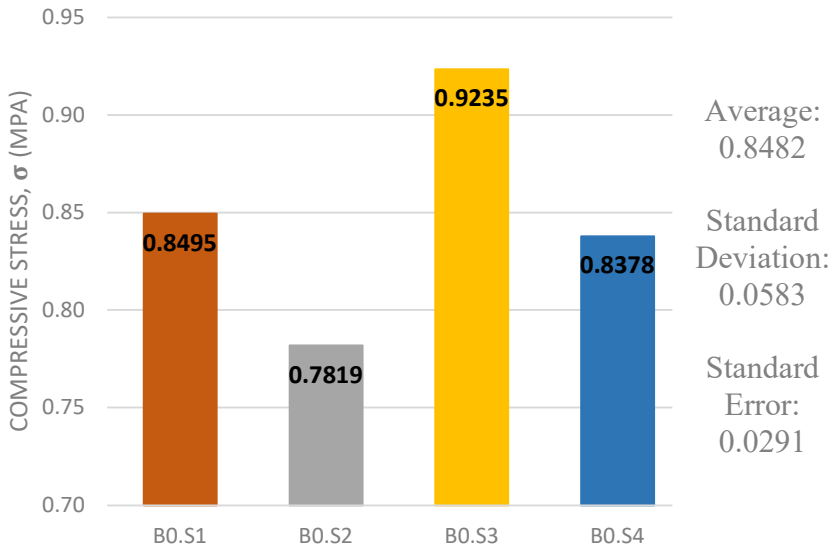

Figure 10. Unconfined compression of samples of batch 0.

On average, the samples of batch 0 (with an average fresh density of 29.6 pcf (4.65 kN/m^3)) have an average uniaxial compressive stress of approximately 0.85 MPa.

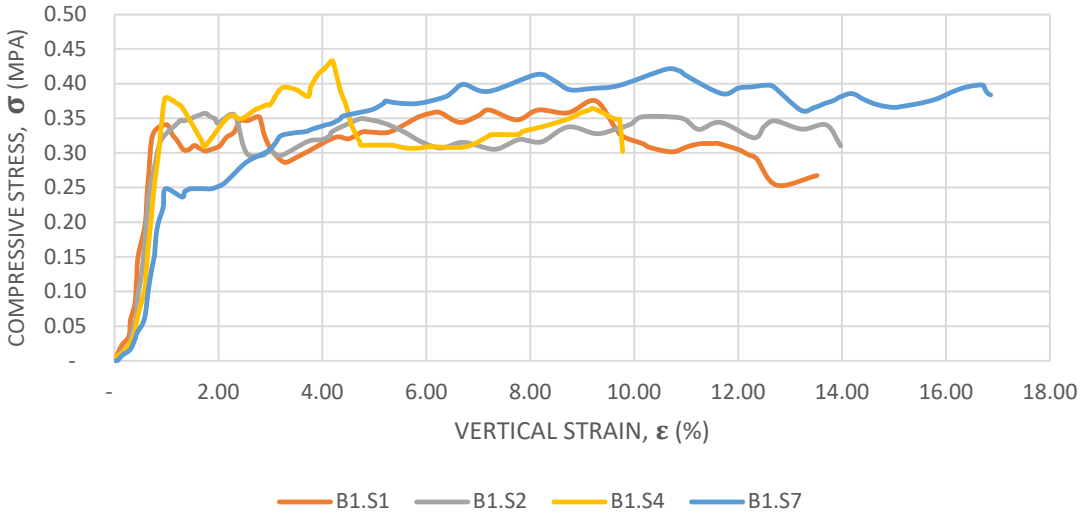

Figure 11. Unconfined compression test graph of batch 1.

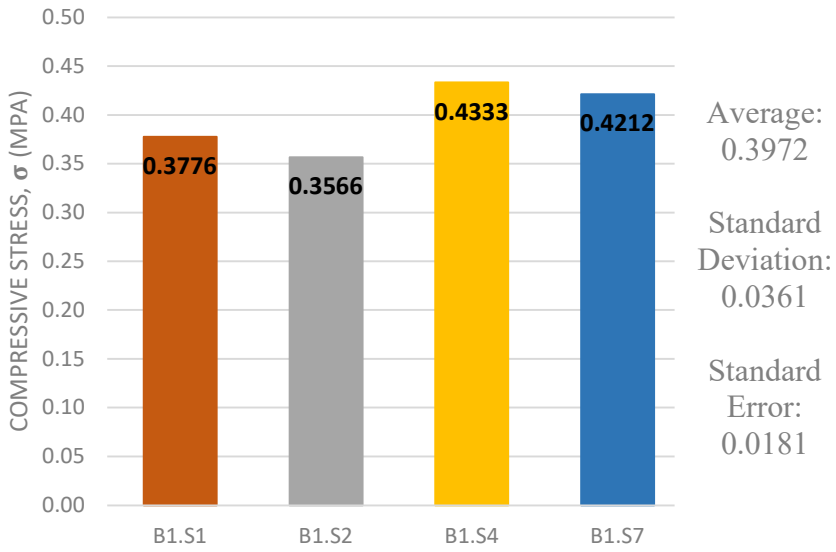

Figure 12. Unconfined compression of samples of batch 1.

On average, the samples of batch 1 (with an average fresh density of 24 pcf (3.77 kN/m^3)) have an average uniaxial compressive stress of 0.40 MPa.

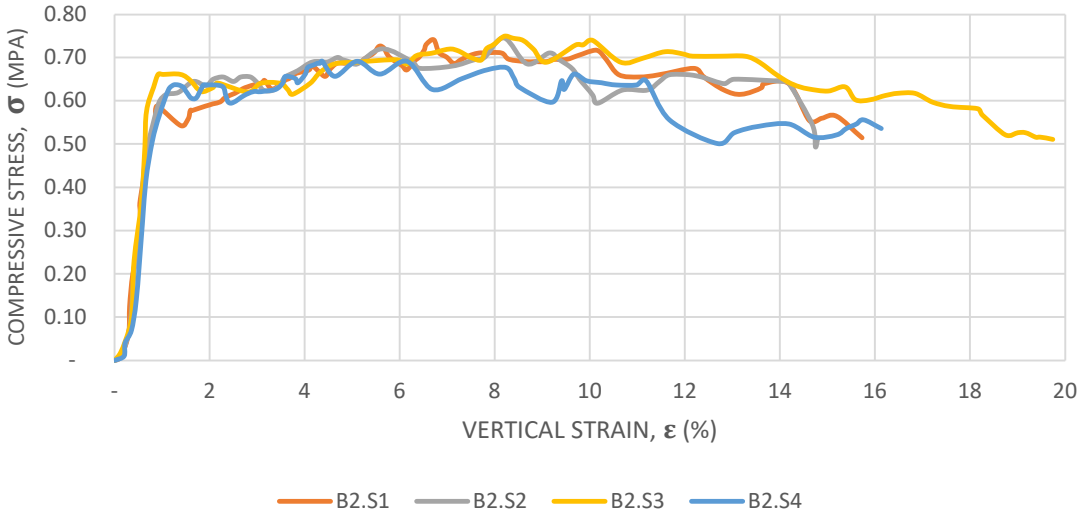

Figure 13. Unconfined compression test graph of batch 2.

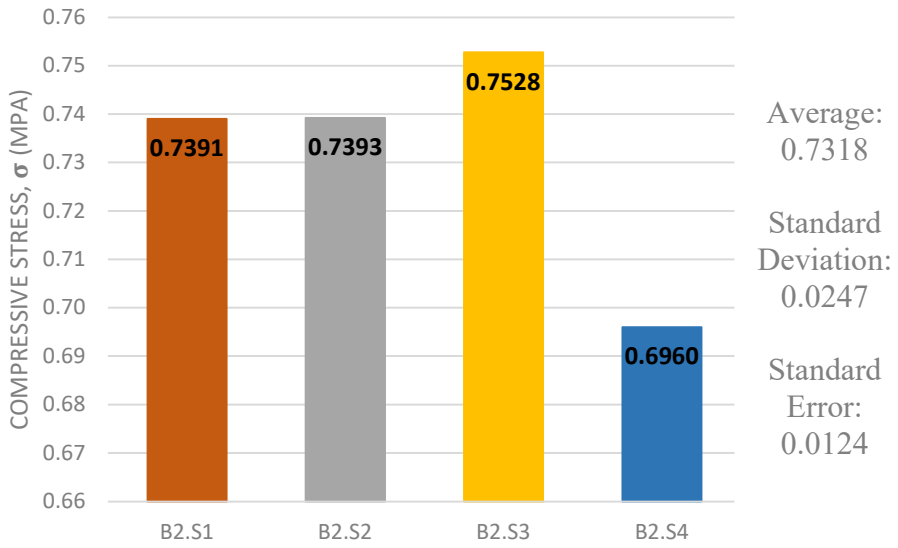

Figure 14. Unconfined compression of samples of batch 2.

On average, the samples of batch 2 (which have an average fresh density of 25.27 pcf (3.97 kN/m^3)) have an average uniaxial compressive stress of approximately 0.73 MPa.

CHAPTER 5

DISCUSSION

Table 3 summarizes the results obtained from the tests discussed in the previous chapters, which are analyzed and compared with other materials described in the literature. This table also tabulates the wet/fresh density of the different batches because density is usually used as a quality index property of Permeable Low-Density Cellular Concrete (PLDCC) attributes.

Resilient Modulus

Kumar [7] analyzed the resilient Modulus of subbase materials and identified the materials' constants, allowing the relationship between resilient Modulus and Bulk Stress. These relationships for PLDCC and other base materials are presented in Tables 3 and 4 and compared graphically in Figure 15.

Bennert [33] analyzed the resilient Modulus of Dense Graded Aggregate Base Course (DGABC) samples of different gradations in a study for developing a performance specification for the granular base and subbase material. The higher modulus value was found in the case of natural gradation in the north of the analyzed region. And the lower resilient modulus value was obtained in the soil gradation classified as the "low end" in the central region.

The resilient module of these extreme DGABC samples, as the Bulk Stress associated with these module values, can be observed in Table 5. This table shows the importance of resilient moduli expected for the PLDCC batches, and the subbase materials analyzed by Kumar (2006), which were calculated through equations 2 to 8, are also presented.

Over the Bulk stresses circumstances of Table 5, it is possible to observe that the PLDCC of batches 0 and 2 reach resilient modulus values close to RBM, which can also be observed in Figure 15. And that these values are, respectively, 11 and 19% higher than the top resilient Modulus of the DGABC samples (158.88 MPa) analyzed by Bennert [33]. Additionally, the resilient Modulus referring to the PLDCC batch 1 on Table 5 also can be accepted as reasonable for subbases applications, besides the slightly lower (3.4%) than the Modulus obtained at the top DGABC sample.

Considering it all, all the PLDCC batches studied reach comparable Resilient Modulus values with other base materials in the stress range of interest. However, it is essential to highlight that the influence of the saturation degree of the PLDCC samples was not explored in this study, which might affect the test results and the conclusion drawn.

Uniaxial Compressive Strength

In a study submitted to Aerix Industries that analyzed Permeable Low-Density Cellular Concrete (PLDCC), it was verified that the compressive strength of dry PLDCC samples of fresh density equal to 25 and 30 pcf (400.46 and 480.55 kg/m3) was reduced in, respectively, 30 and 23% when saturated. Meanwhile, samples with a fresh density

equal to 35 pcf (560.65 kg/m3) did not present any reduction in their compressive strength when saturated [34]. The PLDCC used in this study was made with AQUAERiX-LB foaming agent, which was mixed with water in a 1:50 proportion to produce a foam with a density between 2 to 2.1 pcf (32 to 33.6 kg/m3) that was combined with slurry composed by water and cement in the ratio of 0.50.

The compressive strength of the dry PLDCC samples analyzed by Kevern (2018) and those examined in this study can be observed in Figure 16. This figure shows that Kevern's samples had higher results than the average PLDCC samples of all three batches in this study. This difference appears to be due to minor fractures in the samples of batches 0, 1, and 2, which originated from the resilient modulus test. However, there is the possibility that this reduction is related to the difference in foam density used in each study.

Furthermore, it was observed that the rupture of all the samples of batches 0, 1, and 2 started with the ruin of the sample's bottom, followed by the emergence of fissures in the top direction. Such characteristics can be seen in Figure 17, which shows examples of each batch immediately after the uniaxial compressive test. This behavior was observed in all PLDCC specimens and may be linked to the production process of the samples. During this mixture, it is noticeable that lighter fresh PLDCC was concentrated in the top of the container. And according to the PLDCC laboratory procedure, this more lightweight material was the first layer added to all concrete molds.

Pavement Design Comparison

This section compares the design of regular pavement with one using PLDCC (Permeable Low-Density Cellular Concrete) as a subbase instead of the usual granular material. Both designs consider the Utah Department of Transportation's (UDOT) official traffic count data for Redwood Road between MP 52.401 and MP 53.99, found on this department's website.

Traffic Analysis

Redwood Road's annual average daily traffic (AADT) in 2019 was assumed as a current value for this analysis. This choice was made to avoid historical traffic data conflict due to the global pandemic of 2020. Thus, an amount equal to 52,000 vehicles per day was used to determine the design equivalent single axle load (ESAL), which can be verified in Figure 18.

The pavements analyzed for this roadway were projected for a design life (t) of 20 years, and their overall design can be verified in Table 6. Thus, to predict the traffic growth during this time, the UDOT AADT database was used to determine the growth rate (r) through a trend line, which can be observed in Figure 19.

Then, the value of r was used to determine the growth factor (GY) in Equation 9, and Equations 10 through 13 determined the truck factor (Tf). The summary of the calculation of this factor can be observed in Table 7, where the microstrain values were determined through the Weslea software. Finally, considering all the elements in Table 8, Equation 14 determines each pavement design's ESAL (Nf). This value is also presented in Table 8.

$$GY = \frac{(1+r)^t - 1}{r} \quad \text{[Eq. 9]}$$

$$Trucks = AADT * percent\ trucks_{Su\ or\ CU} * percentFHWA_{class} \quad \text{[Eq. 10]}$$

$$ELF = (\frac{\varepsilon}{\varepsilon_{18\ kip}})^{3.9492} \quad \text{[Eq. 11]}$$

$$ESAL\ Count = \sum trucks * \text{ELF} \quad \text{[Eq. 12]}$$

$$T_f = \frac{Total\ ESALs}{Total\ Trucks} \quad \text{[Eq. 13]}$$

$$\text{Nf} = AADT * 365 * D * L * GY * T * \text{Tf} \quad \text{[Eq. 14]}$$

Distress Modeling

The distress of the pavement designs here analyzed was made using the Pavement Damage Equations for Fatigue Bottom-Up Cracking and Permanent Deformation, which can be found in the Guide for Mechanistic-Empirical Design of Pavement Structures.

Fatigue

Equations 15, 16, and 17 were used to determine the number of load repetitions that result in bottom-up fatigue cracking (Nfc) failure. The result of such equations, and the Miner's relationship between Nf and Nfc, are presented in Table 9.

$$M = 4.84 * (\frac{V_b}{V_a + V_b} - 0.69) \quad \text{[Eq. 15]}$$

$$k'_1 = \frac{1}{0.01 + {}^{12}/_{1 + e^{(15.676 - 2.8186 * h_{AC})}}} \quad \text{[Eq. 16]}$$

$$Nfc = 0.00432 * k'_1 * C * \left(\frac{1}{\varepsilon_t}\right)^{3.9492} * \left(\frac{1}{E}\right)^{1.281} \quad \text{[Eq. 17]}$$

Rutting

Rutting (PD) is a permanent deformation that occurs due to pavement structural failure due to the repetition of loads exceeding the pavement's bearing capacity. This deformation, which occurs cumulative over time, can be calculated following two methods depending on the bound present on each layer's material.

Unbound Material

Pavement's unbound materials are the granular layer's material of the base and subbase. These layers were subdivided into two to obtain a more accurate PD result. Equations 18 to 21 were used for these calculations; the results are presented in Table 10.

$$\log \rho = 0.622685 + 0.541524 * W_c \quad \text{[Eq. 18]}$$

$$\log \beta = -0.61119 - 0.017638 * W_c \quad \text{[Eq. 19]}$$

$$\log(\frac{\varepsilon_0}{\varepsilon_r}) = 0.74168 + 0.08109 * W_c - 0.000012157 * E \quad \text{[Eq. 20]}$$

$$PD = 1.673 * 1.04 * \frac{\varepsilon_0}{\varepsilon_r} * e^{-(\rho/N_f)^{0.7*\beta}} * \varepsilon_v * h_{sub} \quad \text{[Eq. 21]}$$

Bound Material

The material that adheres together, such as the asphalt concrete (mix PG 70-28) used in the pavement designs analyzed in this section, is classified as a bound material. The PLDCC subbase was also considered a bound material. Equations 22 to 25 were used to calculate the PD of these pavement layers; the results are presented in Table 11.

$$C_1 = -0.1039 * {h_{ac}}^2 + 2.4868 * h_{ac} - 17.342 \quad \text{[Eq. 22]}$$

$$C_2 = 0.0172 * {h_{ac}}^2 - 1.7331 * h_{ac} + 27.428 \quad \text{[Eq. 23]}$$

$$k_1 = (C_1 + C_2 * depth) * 0.328196^{depth} \quad \text{[Eq. 24]}$$

$$PD = k_1 * 10^{-3.4488} * T^{1.5606} * {N_f}^{0.479244} * h_{ac} * \varepsilon_r \quad \text{[Eq. 25]}$$

Total Rutting

Following this analysis, the regular pavement's total rutting (PD) equals 0.34 in, a value 26.1% smaller than the one in the pavement design that uses PLDCC as a subbase. However, since the maximum PD allowed in this case was 0.5 in, both pavement designs have been approved for this application with a project life of 20 years. The total rutting of the proposed pavement designs can be observed in Table 12.

Designs Comparison

Both pavement designs can be applied on Redwood Road since the Miner's relationship (Nf/Nfc described in Table 9) in both cases is smaller than 1, indicating that the pavement will not suffer from fatigue cracking along its use. And that the total rutting of both pavements, after 20 years of service, will be smaller than 0.5 inches.

Still, it is essential to note that the pavement with PLDCC as a subbase material has a rutting close to the limit value in this case. In addition, the regular pavement could support an extra 5 years of use and still attend this distress modeling.

Considerations

The tests and analysis in the study described in this paper indicate that the Permeable Low-Density Cellular Concrete (PLDCC) has structural characteristics that allow its use as a pavement subbase or base, in less extreme conditions. Yet, the lack of

focus on details that can strongly influence this material's mechanical characteristics makes highlighting some considerations necessary.

First, all the PLDCC samples analyzed were tested in a dry state. However, the increase in saturation may significantly influence the material's response to the resilient modulus test, as to the uniaxial compressive strength test. It is also valid to mention that this increase also results in a higher complexity at the realization of the mentioned laboratory tests.

Secondly, even with the small number of samples evaluated (12), it was possible to verify that the final product could have highly variable results. This variability can be observed not only in comparing specimens of different batches but also in comparing samples of the same batch. In addition, such variability, which was a decisive factor for the realization of the uniaxial strength tests over the pieces already subjugated to the resilient modulus test, was linked with the procedures for the PLDCC samples production.

The sample production followed the procedures recommended by AERIX Industries to produce PLDCC in the laboratory. During this process, it was observed that lighter PLDCC always gets concentrated on the top of the container where the mixture between the foam and the slurry was made. This more lightweight material was added to the bottom of the concrete molds. Thus, lighter PLDCC was concentrated at the bottom of all samples, the region that first failed at the uniaxial compressive tests.

Finally, this work did not evaluate the influence of environmental factors, such as temperature oscillation. Moreover, there is a need to assess the behavior of the PLDCC as a pavement subbase material from a field perspective.

Table 3. Summary of test results.

Batch	Average Fresh Density		Resilient Modulus Equation		Uniaxial Compressive Strength (MPa)
	(pcf)	(kN/m^2)			
0	29.60	4.65	$MR=9.6674*\theta^{0.5355}$	[Eq. 2]	0.85
1	24.00	3.77	$MR=11.636*\theta^{0.4754}$	[Eq. 3]	0.40
2	25.27	3.97	$MR=11.715*\theta^{0.5125}$	[Eq. 4]	0.73

Table 4. Resilient modulus equation of different subbase materials.

Subbase Material	Resilient Modulus Equation	
Stone dust	$MR=57.566*\theta^{0.0911}$	[Eq. 5]
Fly Ash	$MR=61.011*\theta^{0.1169}$	[Eq. 6]
Coarse sand	$MR=86.338*\theta^{0.0919}$	[Eq. 7]
Riverbed material (RBM)	$MR=29.515*\theta^{0.3369}$	[Eq. 8]

Table 5. Comparison of the resilient modulus of different subbase materials exposed to field bulk stresses.

Material	Bulk Stress, θ (kPa)	Resilient Modulus, MR (MPa)	Bulk Stress, θ (kPa)	Resilient Modulus, MR (MPa)
DGABC, Natural Gradation	227	158.88	254	-
DGABC, Low End		-		126.53
Stone Dust		94.37		95.32
Fly Ash		115.04		116.53
Coarse Sand		142.15		143.59
RBM		183.58		190.53
Batch 0		176.62		187.36
Batch 1		153.43		161.69
Batch 2		188.92		199.90

Table 6. Pavement designs layer's information.

Pavement:	**Regular**			**w/ PLDCC**		
Layer:	Height, h (in):	Resilient Modulus, RM (psi):	Poisson's ratio, v:	Height, h (in):	Resilient Modulus, RM (psi):	Poisson's ratio, v:
Asphalt Concrete	8	405,000	0.35	8	405,000	0.35
Granular Base	8	37,500	0.4	8	37,500	0.4
Granular Subbase	6	9,000	0.4	-	-	-
PLDCC Subbase	-	-	-	6	25,000	0.3
Subgrade	∞	4,500	0.45	∞	4,500	0.45

Table 7. Truck factor (T_f) calculation.

Pavement	**FHWA Class**	**Trucks**	**Microstrain Steer Axle**	**Steer Axle ELF**	**Microstrain Single Axle**	**Single Axle ELF**	**Microstrain Tandem Axle**	**Tandem Axle ELF**	**ESAL Count**	**Truck Factor**
Regular	4	2,962.97	93.17	0.15	120.82	0.42	-	-	1,677.59	0.75
	5	3,555.56	93.17	0.15	150.79	1.00	-	-	4,086.63	
	6	5,333.35	93.17	0.15	-	-	90.00	0.13	1,491.40	
	8	877.70	93.17	0.15	185.52	2.27	91.84	0.14	2,244.91	
	9	585.12	93.17	0.15	-	-	111.66	0.31	444.68	
Total:		13,314.71							9,945.21	
w/ PLDCC	4	2,962.97	88.61	0.16	110.73	0.39	-	-	1,630.91	0.76
	5	3,555.56	88.61	0.16	140.63	1.00	-	-	4,129.31	
	6	5,333.35	88.61	0.16	-	-	85.36	0.14	1,603.16	
	8	877.70	88.61	0.16	172.42	2.24	87.10	0.15	2,236.82	
	9	585.12	88.61	0.16	-	-	105.77	0.32	474.35	
Total:		13,314.71							10,074.54	

Table 8. Design equivalent single axle load (ESAL) calculation.

Pavement:	Regular	w/ PLDCC
Average Annual Daily Traffic (AADT)	52,053	
Lane Factor (L)	0.8	
Direction Factor (D)	0.5	
Percent of Trucks (T)	25.6%	
Growth Rate (r)	1%	
Project Life, years (t)	20	
Growth Factor (GY)	20.02	
Truck Factor (T_f)	0.75	0.76
Design ESAL (Nf)	31,997,684	32,413,794

Table 9. Design equivalent single axle load (ESAL) calculation.

Pavement:	Regular	w/ PLDCC
V_a	6	
V_b	12	
K'_1	250	
Elastic Modulus of the First Layer (E)	405,000	
Strain Under the First Layer (ε_t)	$150.79 * 10^{-6}$	$140.63 * 10^{-6}$
M	-0.113	
C	0.771	
Nfc	67,563,431	88,992,005
Nf/Nfc	0.47	0.36

Table 10. Summary of values and calculation of the rutting in granular layers.

Pavement	**Regular**				**w/ PLDCC**	
Granular Sublayer	**Base 1**	**Base 2**	**Subbase 1**	**Subbase 2**	**Base 1**	**Base 2**
Nf	**31,997,684**				**32,413,794**	
Wc (%)	**12**				**12**	
E (psi)	**37,500**		**9,000**		**37,500**	
h (in)	**4**		**3**		**4**	
β_{GB}	**1.673**				**1.673**	
$\log(\frac{\varepsilon_0}{\varepsilon_r})$	**1.2589**		**1.6053**		**1.2589**	
M_r/1000	**37.50**		**9.00**		**37.50**	
Adj. Strain Ratio	**1.0421**		**0.3753**		**1.0421**	
Adj. Ratio*$(\frac{\varepsilon_0}{\varepsilon_r})$	**18.9137**		**15.1247**		**18.9137**	
Log(β)	**-0.8228**				**-0.8228**	
Corrected β	**0.1053**				**0.1053**	
Log(ρ)	**7.1210**				**7.1210**	
ρ	**$1.32*10^7$**				**$1.32*10^7$**	
$(\rho/N)^{\beta}$	**0.911**				**0.911**	
$e^{-(\rho/N)\beta}$	**0.402**				**0.402**	
$\frac{\varepsilon_\rho}{\varepsilon_v}$	**12.72**		**10.17**		**12.74**	
ε_ρ	**0.00311**	**0.00284**	**0.00352**	**0.00324**	**0.00179**	**0.00153**
ε_r	**244.58**	**223.47**	**346.20**	**318.25**	**140.25**	**120.06**
PD (in)	**0.0124**	**0.0114**	**0.0106**	**0.0097**	**0.0071**	**0.0061**

Table 11. Summary of values and calculation of the rutting in bounded layers.

Pavement	**Regular**	**w/ PLDCC**	
Layer	Asphalt Concrete	Asphalt Concrete	PLDCC Subbase
Microstrain, ε_r	112.86	105.47	65.82
h_{ac} (in)	8	8	6
Depth (in)	4	4	4
C_1	14.66	14.66	17.65
C_2	-4.10	-4.10	-6.16
Nf	31,997,684	32,413,794	32,413,794
T	45	45	45
k_1	0.63	0.63	0.75
ε_p	0.04	0.04	0.03
$\varepsilon_p/\varepsilon_r$	338.36	340.47	402.08
PD (in)	0.3055	0.2873	0.1588

Table 12. Total rutting of the analyzed pavements.

Pavement	Regular	w/ PLDCC
Layers:		
Asphalt Concrete	0.3055	0.2873
Granular Base	0.0238	0.0132
Granular Subbase	0.0203	-
PLDCC Subbase	-	0.1588
Total (in):	0.34	0.46

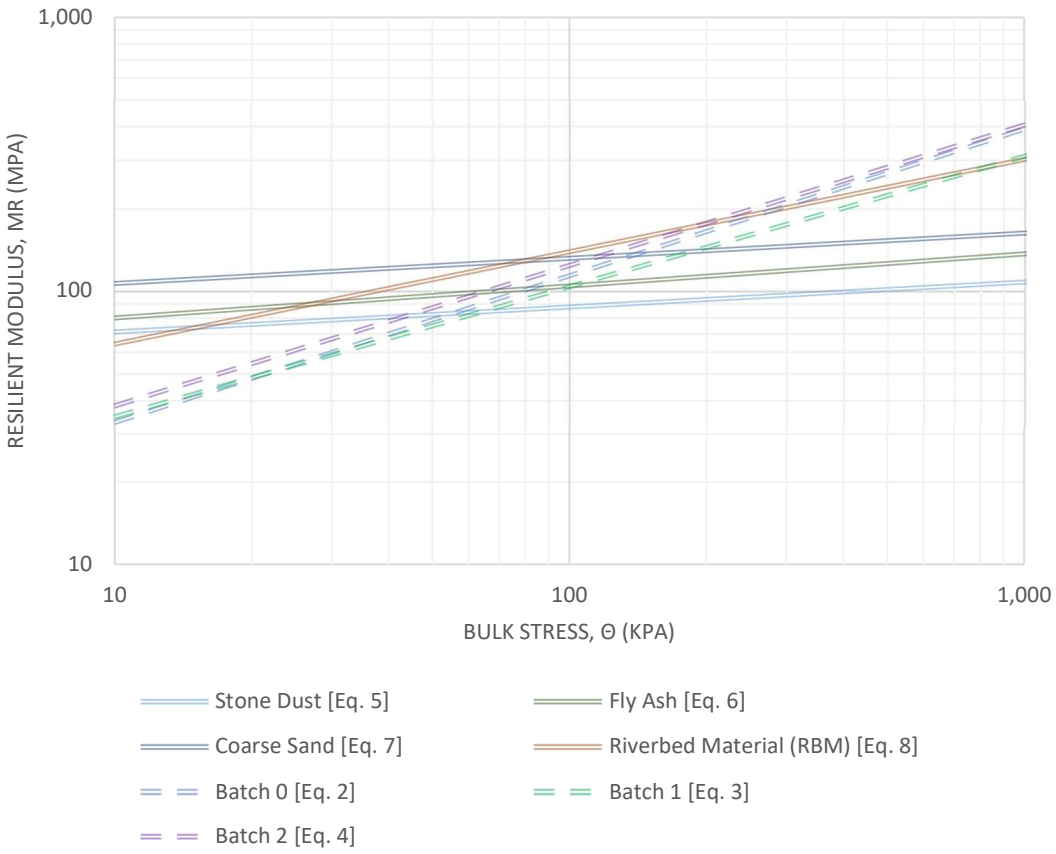

Figure 15. Graph of the Bulk Stress versus the Resilient Modulus of subbase materials and the PLDCC batches.

For values lower than 100 kPa of the Bulk Stress, the Resilient Modulus of PLDCC is 30 to 40 MPa, which is lower than other subgrade materials. However, when the Bulk Stress is between 100 to 200 kPa, a usual range for road bases undergoing dead and heavy truck live tire loads, PLDCC Resilient Modulus is comparable to or higher than other subgrade materials analyzed by Kumar (2006).

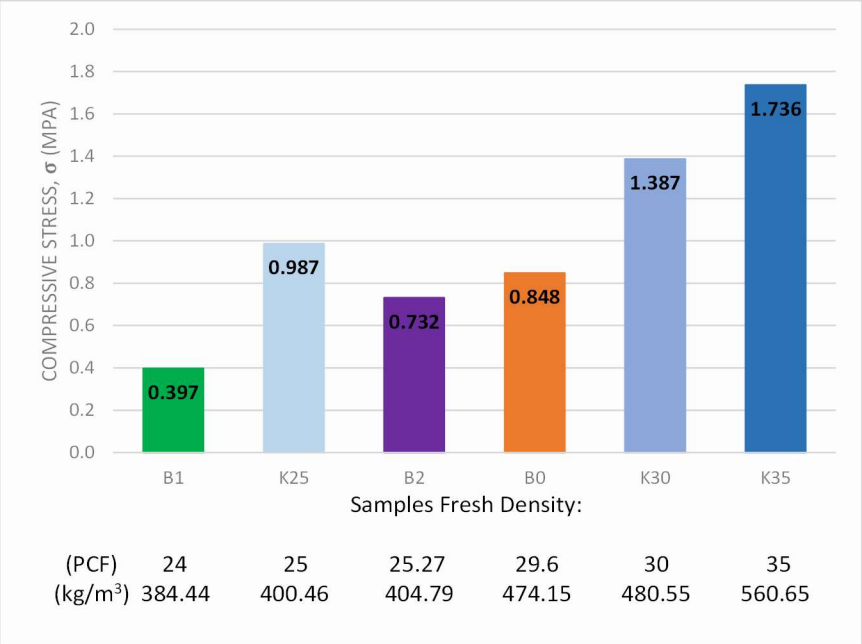

Figure 16. Compressive strength of dry PLDCC samples of different fresh densities.

K25, K30, and K35 are the uniaxial compressive strength values Kevern (2018) identified. B0, B1, and B2 are the average values of the samples of the batches analyzed in this study.

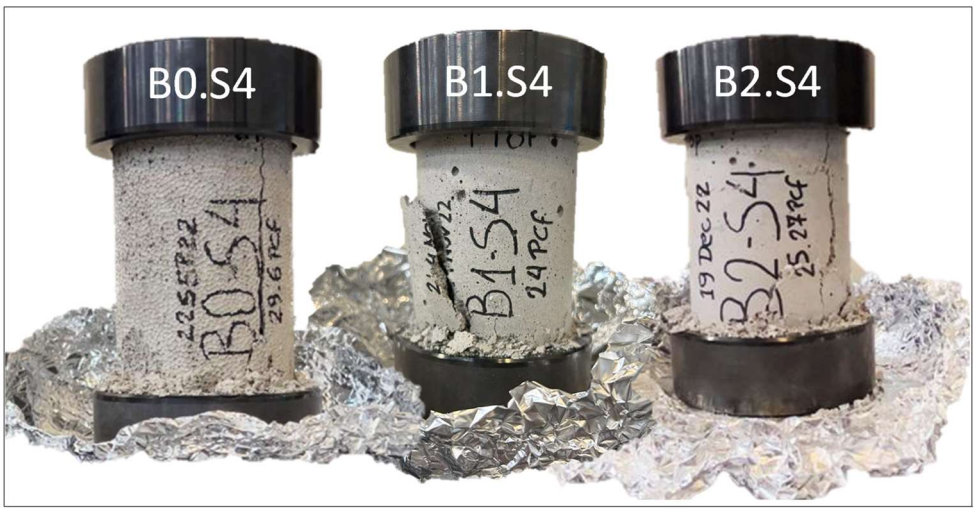

Figure 17. Samples of each batch immediately after the uniaxial compressive strength test.

Sample number 4 of each batch is presented in this picture as a rupture reference for each set.

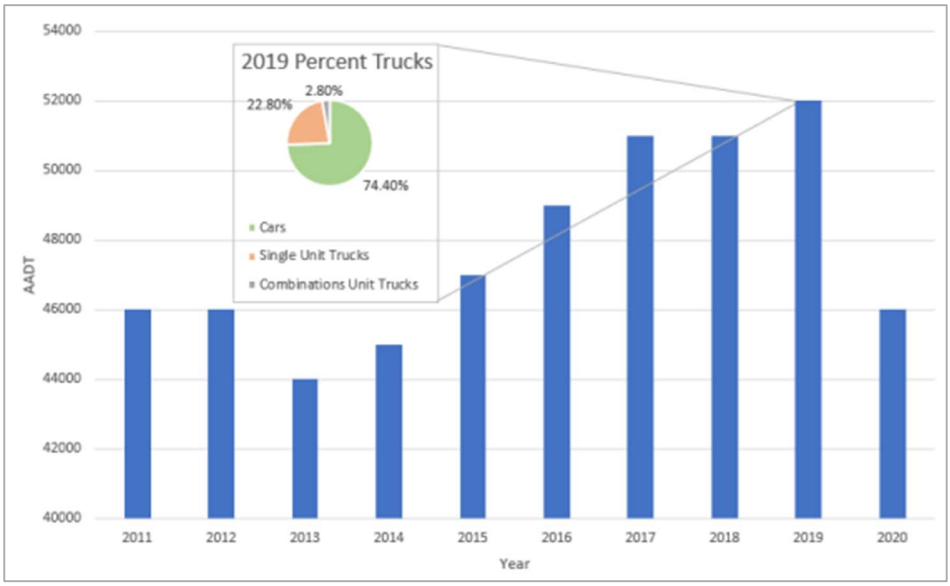

Figure 18. Historic AADT on Redwood Road registered on UDOT.

From this figure, it is possible to notice that the pandemic strongly influenced the AADT of this region, as the different categories of vehicles of the total AADT in the year 2019.

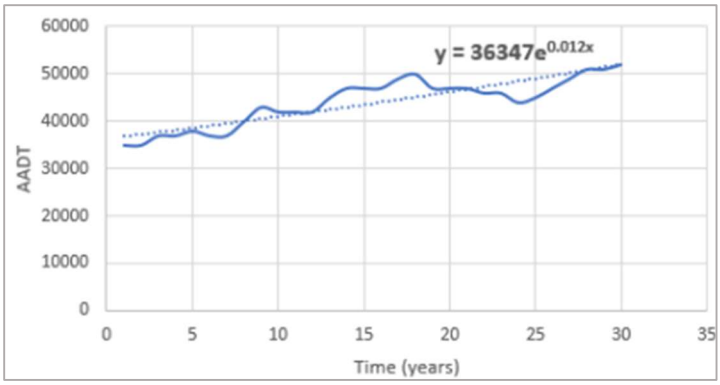

Figure 19. Redwood Road's annual average daily traffic (AADT) between 1990 and 2019.

The trendline equation in the figure shows a growth rate (r) equal to 0.012. This value is approximately 1% for the analysis made in this section.

CHAPTER 6

CONCLUSION

This research evaluated the mechanical properties of permeable low-density cellular concrete (PLDCC) to determine the viability of using PLDCC as a pavement subbase material. We conducted Resilient Modulus (RM) and uniaxial compressive (UC) strength tests using samples of PLDCC at different densities to fulfill this objective. The results of the RM and UC tests indicate acceptable ranges for this application for subbase materials for conventional flexible pavement systems. This conclusion was tested by comparing evaluations from mechanistic-empirical pavement design that implemented PLCC and other subbase materials.

In short, our research results show that the PLDCC's mechanical properties make it a viable alternative to granular subbases of traditional flexible pavement systems. The properties we evaluated suggest the feasibility of using PLDCC as an alternative subbase material, especially where drainage and water storage capabilities are desired in the roadway system.

The RM behavior is stress-dependent; this modulus increases significantly with increasing bulk stress. We found that the PLDCC's RM, when subjected to levels of bulk stress typically found in pavement subbases (i.e., in situ bulks stress levels greater than 100 kPa), is equal to or higher than the RM of other subbase materials, such as stone dust,

coarse sand, fly ash. At high-stress levels, only riverbed materials produce comparable RM values (Figure 15).

However, the PLDCC samples analyzed for uniaxial compressive strength (UCS) showed smaller values than those obtained by Kevern [34]. Nonetheless, the range of uniaxial compressive strength for the analyzed samples is in the acceptable range for subbase materials.

We believe significant variability in the PLDCC RM and UCS values may result from sample size effects, production methods (i.e., laboratory specimens versus field installation), and environmental factors. For example, the field installation of PLDCC differs considerably from the method used in the laboratory. It is possible that a field-installed PLDCC produces a higher quality material due to better mixing of the foam and the slurry during the in-line mixing and pumping process. However, this variability of PLDCC in field applications needs to be explored in future work. In addition, the degree of saturation of the PLDCC and possible chemical interactions with contaminated or acidic water may affect PLDCC's long-term physical properties for applications where groundwater or surface water encroaches into its matrix. We encourage this and other environmental factors to be explored in future research.

APPENDIX A

RESILIENT MODULUS TEST REPORTS

Resilient Modulus Test Data

Summary Report

Sample: **B0-S1**

MR = 2,825.8 * B $^{0.6654}$ r = 0.96182

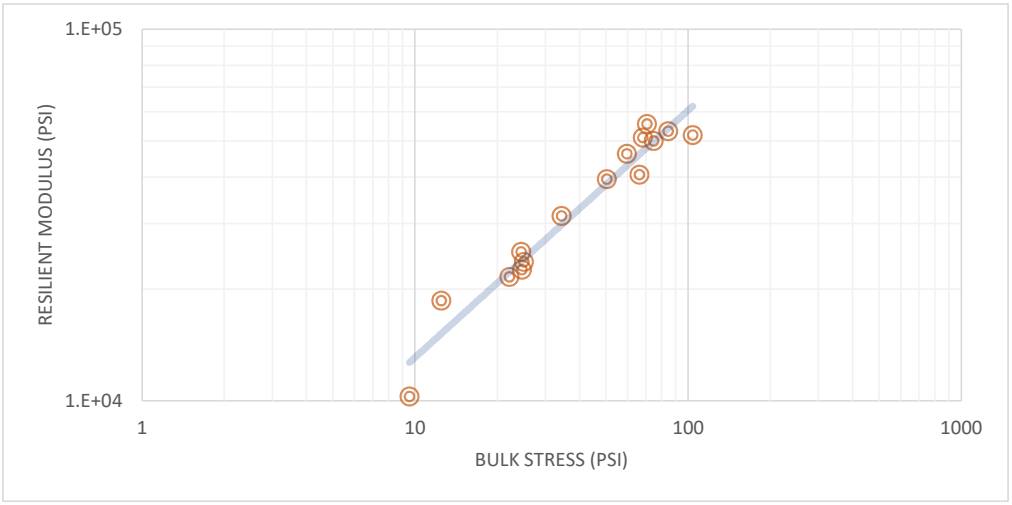

Test Date: 01/13/2023

Confining Stress, S3 (psi)	Nom. Max. Deviator Stress (psi)	Mean Deviator Stress (psi)	Std. Dev. Deviator Stress (psi)	Mean Bulk Stress (psi)	Mean Resilient Strain (%)	Std. Dev. Resilient Strain (%)	Mean Resilient Modulus (psi)	Std. Dev. Resilient Modulus (psi)
3.198	3	-0.04671	0.1720	9.549	0.00	0.00	10252	670.0
3.033	6	3.379	3.9375	12.48	0.02	0.02	18582	1,222.5
3.041	9	15.32	7.2000	24.44	0.06	0.03	25112	1,300.5
5.197	5	9.428	4.5853	25.02	0.04	0.02	23617	440.9
4.875	10	9.984	1.4420	24.61	0.04	0.01	22515	275.8
4.989	15	7.219	0.6999	22.18	0.03	0.00	21495	642.0
10.14	10	3.984	0.8502	34.39	0.01	0.00	31427	1,420.4
10.21	20	19.75	2.8994	50.37	0.05	0.01	39420	897.0
9.95	30	29.87	2.6294	59.72	0.06	0.00	46185	1,679.9
14.89	10	10.62	4.5896	66.28	0.03	0.01	40543	2,100.4
15.17	15	22.666	3.0929	68.17	0.04	0.00	51017	2,396.3
14.96	30	29.92	3.9326	74.81	0.06	0.01	49986	1,418.4
20.01	15	10.7	4.8921	70.73	0.02	0.01	55571	4,293.0
20.07	20	24.26	4.6967	84.48	0.04	0.01	53086	3,642.2
20.01	40	43.82	5.1144	103.9	0.08	0.01	51843	437.6

Figure 20. Resilient modulus test data of sample 1 of batch 0 (B0-S1).

Resilient Modulus Test Data
Summary Report
Sample: **B0-S2**

MR = 3,953.7 * B $^{0.5117}$ r = 0.96840

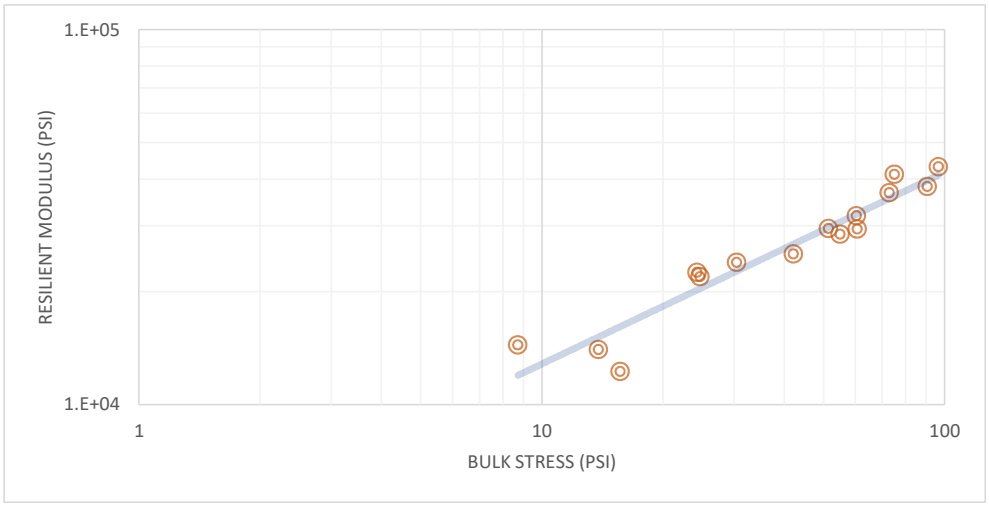

Test Date: 01/13/2023

Confining Stress, S3 (psi)	Nom. Max. Deviator Stress (psi)	Mean Deviator Stress (psi)	Std. Dev. Deviator Stress (psi)	Mean Bulk Stress (psi)	Mean Resilient Strain (%)	Std. Dev. Resilient Strain (%)	Mean Resilient Modulus (psi)	Std. Dev. Resilient Modulus (psi)
2.985	3	-0.2292	0.0855	8.726	0.00	0.00	14429	243.7
3.357	6	3.759	3.2626	13.83	0.02	0.02	14036	760.5
3.029	9	15.21	6.7613	24.29	0.07	0.03	22536	122.8
5.156	5	0.195	0.2745	15.66	0.00	0.00	12260	699.2
4.967	10	9.83	1.7175	24.73	0.05	0.01	21946	245.6
5.143	15	15.04	0.1652	30.47	0.06	0.00	23971	162.6
10.3	10	11.29	2.7683	42.18	0.04	0.01	25212	1,491.1
10.18	20	20.98	3.2353	51.51	0.07	0.01	29486	488.3
10.14	30	30.02	0.0390	60.45	0.09	0.00	31916	60.8
15.06	10	9.881	0.2620	55.05	0.04	0.00	28475	360.8
15.27	15	14.94	0.7441	60.74	0.05	0.00	29414	241.9
15.16	30	27.36	3.0460	72.85	0.07	0.01	36775	948.2
20.05	15	14.91	0.6292	75.07	0.04	0.00	41175	680.0
19.92	20	30.87	2.1604	90.63	0.08	0.00	38192	1,151.7
20.02	40	36.53	6.3928	96.59	0.08	0.01	43132	892.1

Figure 21. Resilient modulus test data of sample 2 of batch 0 (B0-S2).

Resilient Modulus Test Data

Summary Report

Sample: **B0-S3**

MR = 1,094.2 * B $^{0.8325}$ r = 0.94805

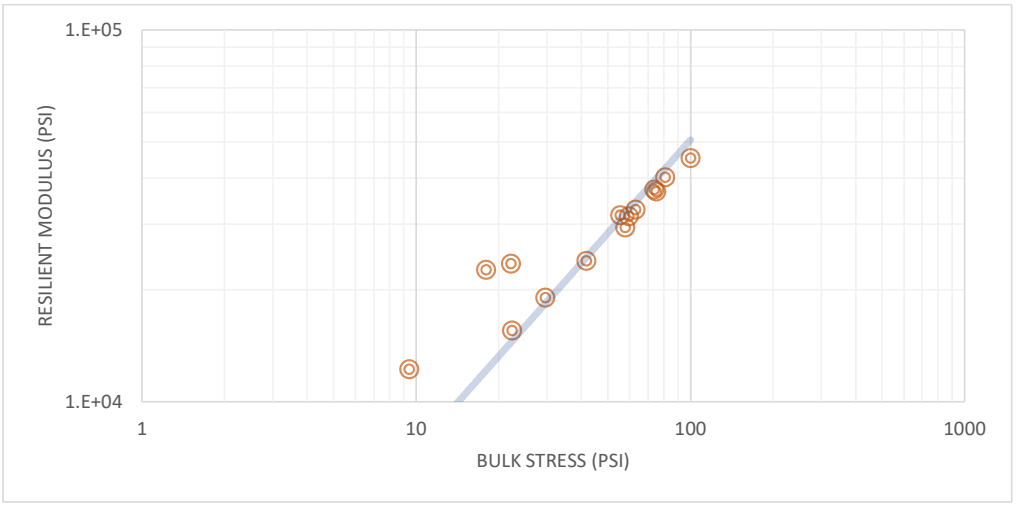

Test Date: 01/14/2023

Confining Stress, S3 (psi)	Nom. Max. Deviator Stress (psi)	Mean Deviator Stress (psi)	Std. Dev. Deviator Stress (psi)	Mean Bulk Stress (psi)	Mean Resilient Strain (%)	Std. Dev. Resilient Strain (%)	Mean Resilient Modulus (psi)	Std. Dev. Resilient Modulus (psi)
2.992	3	0.4609	1.4804	9.437	0.01	0.01	12205	982.2
2.946	6	-0.1337	0.0897	8.704	0.00	0.00	1887	-
3.131	9	13	4.0501	22.39	0.08	0.02	15519	892.3
5.167	5	2.501	4.2175	18	0.01	0.02	22607	2,809.8
5.115	10	6.815	4.0319	22.16	0.03	0.02	23485	1,177.0
5.553	15	12.91	0.5610	29.57	0.07	0.00	19014	499.0
10.05	10	11.66	0.3716	41.8	0.05	0.00	23889	347.5
10.25	20	27.06	1.4074	57.83	0.09	0.00	29374	892.3
10.03	30	29.63	0.1224	59.72	0.09	0.00	31482	159.0
15.12	10	10.19	0.6566	55.55	0.03	0.00	31719	550.5
15.19	15	17.62	0.7173	63.2	0.05	0.00	32836	405.6
15.14	30	29.75	3.5061	75.16	0.08	0.01	36729	1,463.4
19.92	15	14.14	4.8916	73.9	0.04	0.01	37163	2,239.1
20.01	20	20.93	1.7583	80.96	0.05	0.00	40099	314.3
19.85	40	40.51	5.6885	100.1	0.09	0.01	45153	759.4

Figure 22. Resilient modulus test data of sample 3 of batch 0 (B0-S3).

Resilient Modulus Test Data
Summary Report
Sample: **B0-S4**

MR = 5,296.5 * B $^{0.4603}$ r = 0.93622

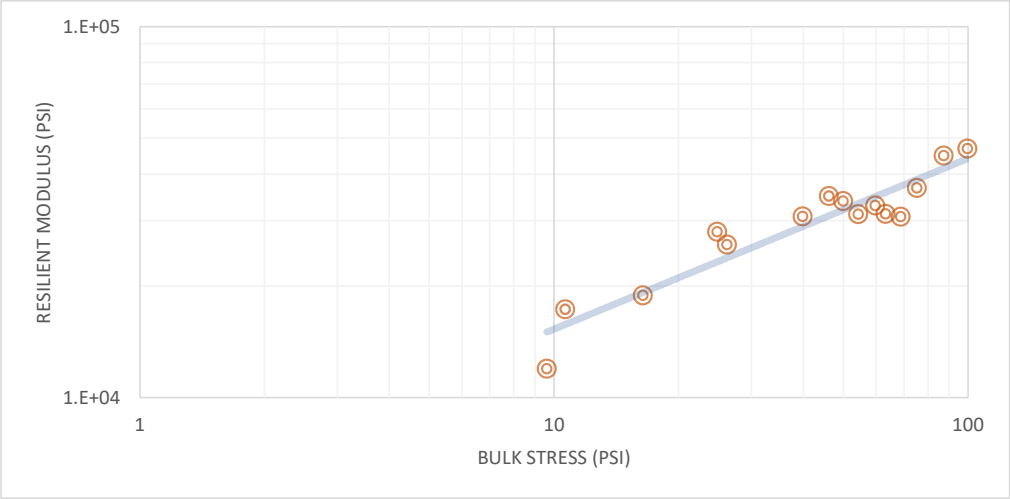

Test Date: 01/14/2023

Confining Stress, S3 (psi)	Nom. Max. Deviator Stress (psi)	Mean Deviator Stress (psi)	Std. Dev. Deviator Stress (psi)	Mean Bulk Stress (psi)	Mean Resilient Strain (%)	Std. Dev. Resilient Strain (%)	Mean Resilient Modulus (psi)	Std. Dev. Resilient Modulus (psi)
3.297	3	-0.2675	0.0716	9.623	0.00	0.00	11962	1,223.8
3.18	6	1.105	1.4216	10.65	0.01	0.01	17307	1,826.3
2.995	9	17.22	6.8833	26.2	0.07	0.02	25860	130.2
4.968	5	1.51	1.8806	16.42	0.01	0.01	18849	2,469.0
5.068	10	9.605	6.2899	24.81	0.04	0.02	27958	965.1
5.014	15	24.83	0.7080	39.88	0.08	0.00	30759	199.0
9.999	10	16.13	1.0104	46.13	0.05	0.00	34894	301.1
10.03	20	19.85	2.8147	49.93	0.06	0.01	33855	349.5
10.09	30	29.48	2.4726	59.77	0.09	0.01	32911	1,145.2
15.06	10	9.178	0.5206	54.37	0.03	0.00	31223	243.9
15.05	15	18.07	4.0016	63.23	0.06	0.01	31245	858.2
15.04	30	30.21	3.7148	75.32	0.08	0.01	36749	2,377.1
19.85	15	9.281	4.1064	68.82	0.03	0.01	30749	4,048.7
19.96	20	27.5	2.2732	87.39	0.06	0.00	44907	1,759.1
20.01	40	39.67	4.7052	99.71	0.08	0.01	46866	560.0

Figure 23. Resilient modulus test data of sample 4 of batch 0 (B0-S4).

Resilient Modulus Test Data
Summary Report
Sample: **B1-S1**

MR = 2,052.7 * B $^{0.6656}$ r = 0.95833

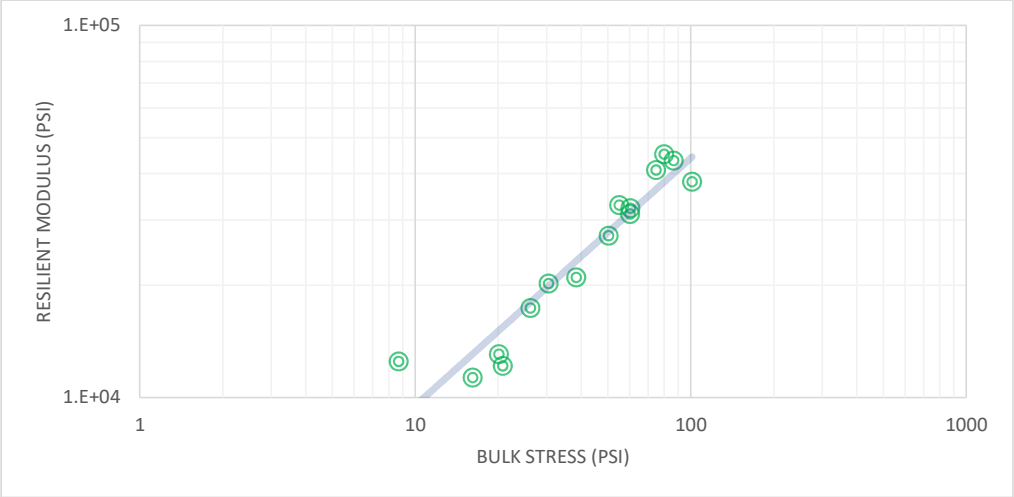

Test Date: 01/07/2023

Confining Stress, S3 (psi)	Nom. Max. Deviator Stress (psi)	Mean Deviator Stress (psi)	Std. Dev. Deviator Stress (psi)	Mean Bulk Stress (psi)	Mean Resilient Strain (%)	Std. Dev. Resilient Strain (%)	Mean Resilient Modulus (psi)	Std. Dev. Resilient Modulus (psi)
2.99	3	-0.269	0.0171	8.702	0.00	0.00	12460	1,294.8
2.981	6	11.83	3.6822	20.77	0.10	0.02	12122	347.1
2.978	9	11.18	5.4249	20.12	0.09	0.04	13037	267.5
5.069	5	0.9385	0.8725	16.15	0.01	0.01	11285	1,051.7
5.196	10	10.6	0.4628	26.19	0.06	0.00	17344	183.1
5.041	15	15.31	0.1564	30.43	0.07	0.00	20192	132.3
10.14	10	7.934	0.9206	38.34	0.04	0.00	20992	300.6
10.06	20	20.09	0.9153	50.28	0.07	0.00	27157	94.3
10.16	30	29.86	0.2685	60.33	0.09	0.00	32243	236.0
14.98	10	9.987	0.5458	54.94	0.03	0.00	32852	980.7
15.05	15	15.1	3.3636	60.26	0.05	0.01	31060	658.0
15	30	29.87	2.3871	74.86	0.07	0.01	40808	549.0
20.23	15	25.93	1.1372	86.6	0.06	0.00	43242	760.0
20.05	20	19.84	0.0706	80.09	0.04	0.00	44997	239.7
20.28	40	40.27	4.3636	101.1	0.10	0.01	37924	651.5

Figure 24. Resilient modulus test data of sample 1 of batch 1 (B1-S1).

Resilient Modulus Test Data
Summary Report
Sample: **B1-S2**

MR = 2,774.3 * B $^{0.5434}$ r = 0.98742

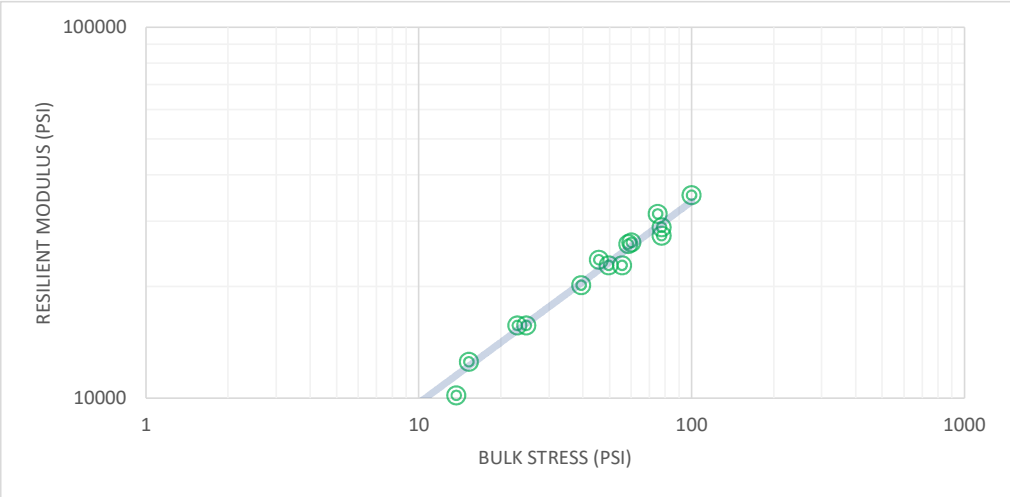

Test Date: 01/13/2023

Confining Stress, S3 (psi)	Nom. Max. Deviator Stress (psi)	Mean Deviator Stress (psi)	Std. Dev. Deviator Stress (psi)	Mean Bulk Stress (psi)	Mean Resilient Strain (%)	Std. Dev. Resilient Strain (%)	Mean Resilient Modulus (psi)	Std. Dev. Resilient Modulus (psi)
2.729	3	-0.06757	0.2305	8.118	0.00	0.00	9305	461.1
3.527	6	4.721	3.6558	15.3	0.04	0.02	12529	1,030.7
2.881	9	5.119	7.4964	13.76	0.04	0.05	10167	716.6
5.17	5	7.506	3.6580	23.02	0.05	0.02	15693	883.8
5.035	10	9.745	5.9917	24.85	0.06	0.03	15698	1,516.7
4.932	15	24.7	1.0667	39.5	0.12	0.00	20153	257.7
9.988	10	15.87	1.7333	45.84	0.07	0.01	23587	521.9
10.04	20	19.68	0.9395	49.8	0.08	0.00	22808	142.2
10.12	30	29.84	0.1093	60.21	0.11	0.00	26274	136.0
15.07	10	10.52	0.1109	55.71	0.05	0.00	22774	117.7
15.09	15	13.43	1.1137	58.69	0.05	0.00	26007	941.9
15.14	30	29.82	0.1084	75.24	0.09	0.00	31350	308.6
19.89	15	18.08	3.3575	77.75	0.06	0.01	28882	1,506.9
19.97	20	17.92	2.6495	77.84	0.06	0.00	27397	1,920.7
20.07	40	39.87	3.2738	100.1	0.11	0.01	35232	604.0

Figure 25. Resilient modulus test data of sample 2 of batch 1 (B2-S1).

Resilient Modulus Test Data
Summary Report
Sample: **B1-S4**

MR = 7,446.4 * B $^{0.3336}$ r = 0.89894

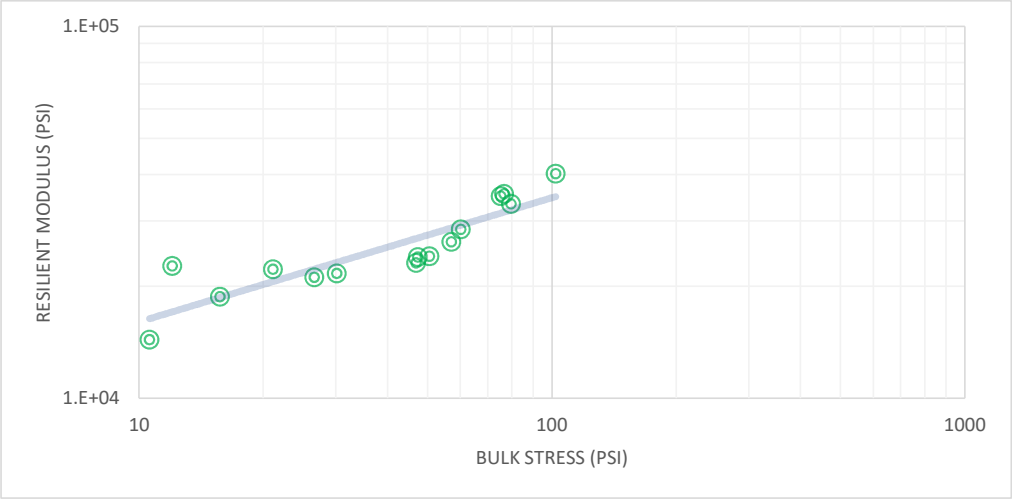

Test Date: 01/07/2023

Confining Stress, S3 (psi)	Nom. Max. Deviator Stress (psi)	Mean Deviator Stress (psi)	Std. Dev. Deviator Stress (psi)	Mean Bulk Stress (psi)	Mean Resilient Strain (%)	Std. Dev. Resilient Strain (%)	Mean Resilient Modulus (psi)	Std. Dev. Resilient Modulus (psi)
2.689	3	2.532	3.2525	10.6	0.01	0.02	14386	1,092.7
2.9	6	3.356	5.6856	12.05	0.02	0.03	22686	1,289.4
3.08	9	11.89	4.7233	21.13	0.06	0.02	22237	1,172.8
5.222	5	0.04677	0.6499	15.71	0.00	0.00	18754	1,001.1
4.967	10	15.25	0.2412	30.15	0.07	0.00	21679	158.5
5.113	15	11.25	1.7633	26.59	0.05	0.01	21166	394.5
10.27	10	16.51	2.1461	47.33	0.07	0.01	23964	819.9
10.19	20	20	3.8043	50.56	0.08	0.01	24112	1,120.7
10.2	30	29.58	3.7819	60.18	0.10	0.01	28451	699.9
14.77	10	2.635	1.1687	46.94	0.01	0.00	23140	2,678.7
15.19	15	11.5	3.1438	57.08	0.04	0.00	26324	339.0
15.25	30	29.49	1.6110	75.23	0.08	0.00	34963	277.4
20	15	16.62	4.7603	76.61	0.05	0.02	35431	2,437.7
20.11	20	19.28	1.1573	79.62	0.06	0.00	33342	879.8
20.04	40	42.01	4.9015	102.1	0.10	0.01	40180	1,393.3

Figure 26. Resilient modulus test data of sample 4 of batch 1 (B4-S1).

Resilient Modulus Test Data
Summary Report
Sample: **B1-S7**

MR = 8,178.5 * B $^{0.336}$ r = 0.90719

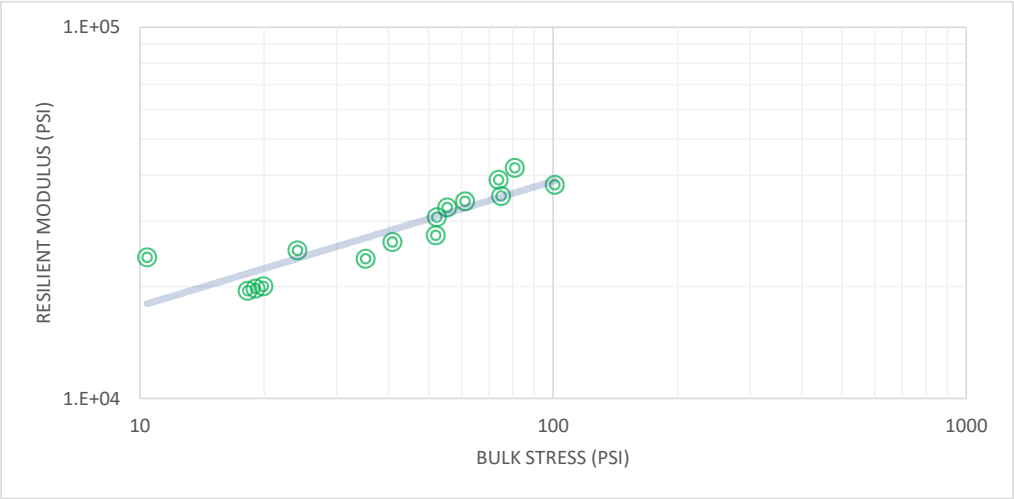

Test Date: 01/07/2023

Confining Stress, S3 (psi)	Nom. Max. Deviator Stress (psi)	Mean Deviator Stress (psi)	Std. Dev. Deviator Stress (psi)	Mean Bulk Stress (psi)	Mean Resilient Strain (%)	Std. Dev. Resilient Strain (%)	Mean Resilient Modulus (psi)	Std. Dev. Resilient Modulus (psi)
3.588	3	-0.34	0.0148	10.43	0.00	0.00	23952	1,710.0
3.347	6	9.888	6.3393	19.93	0.05	0.03	20014	863.9
3.259	9	8.477	6.3249	18.26	0.05	0.03	19478	1,098.6
5.558	5	7.414	3.9930	24.09	0.03	0.02	25024	1,577.2
2.487	10	2.601	1.7680	19.06	0.01	0.01	19749	1,875.5
5.336	15	19.22	2.5182	35.23	0.08	0.01	23783	104.9
10.5	10	9.386	2.9548	40.87	0.04	0.01	26345	434.1
10.72	20	19.84	4.8695	52.02	0.07	0.01	27499	1,912.0
10.47	30	29.87	3.6712	61.28	0.09	0.01	33923	766.7
15.2	10	9.86	0.5614	55.46	0.03	0.00	32669	462.3
15.1	15	7.1	3.4054	52.39	0.02	0.01	30759	897.2
15.03	30	29.85	4.2399	74.94	0.08	0.01	35082	2,045.0
20.27	15	13.09	0.3237	73.9	0.03	0.00	38793	523.1
20.31	20	19.94	1.5430	80.88	0.05	0.00	41759	461.8
20.28	40	40.14	4.1859	101	0.10	0.01	37575	1,583.7

Figure 27. Resilient modulus test data of sample 7 of batch 1 (B7-S1).

Resilient Modulus Test Data
Summary Report
Sample: **B2-S1**

MR = 6,416.5 * B $^{0.4229}$ r = 0.97601

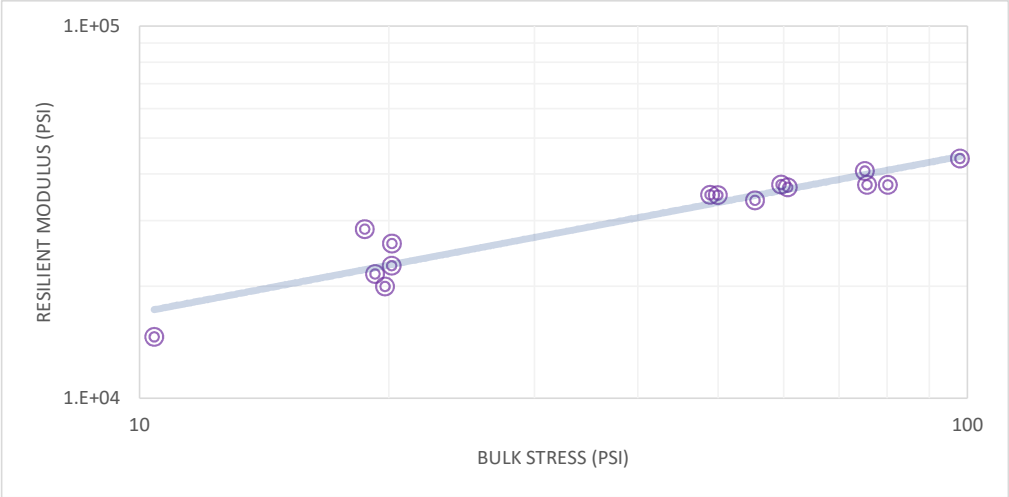

Test Date: 01/14/2023

Confining Stress, S3 (psi)	Nom. Max. Deviator Stress (psi)	Mean Deviator Stress (psi)	Std. Dev. Deviator Stress (psi)	Mean Bulk Stress (psi)	Mean Resilient Strain (%)	Std. Dev. Resilient Strain (%)	Mean Resilient Modulus (psi)	Std. Dev. Resilient Modulus (psi)
2.603	3	2.611	3.9463	10.42	0.02	0.02	14602	1132.4
3.03	6	10.17	5.3077	19.26	0.05	0.02	21533	1889.1
2.887	9	11.5	4.5421	20.16	0.05	0.02	22683	2029.7
5.12	5	3.355	3.9304	18.71	0.02	0.02	28419	3910.2
5.056	10	5.014	5.7239	20.18	0.02	0.02	26009	976.2
5.035	15	4.686	0.2413	19.79	0.02	0.00	19925	552.0
10.23	10	18.23	1.0384	48.92	0.05	0.00	35163	286.1
10.11	20	19.65	4.7625	49.99	0.06	0.01	35128	231.8
10.14	30	30.29	5.1099	60.71	0.08	0.01	36836	1148.9
15.19	10	9.84	4.0349	55.4	0.03	0.01	33956	1477.7
15.1	15	14.27	3.6790	59.57	0.04	0.01	37482	1208.5
15.17	30	29.69	7.2233	75.21	0.07	0.02	40717	482.7
20.22	15	15.03	5.2061	75.69	0.04	0.01	37376	2783.1
20.01	20	20.17	5.2821	80.21	0.06	0.02	37429	1148.9
20.01	40	37.97	8.5568	98.02	0.08	0.02	43999	1477.7

Figure 28. Resilient modulus test data of sample 1 of batch 2 (B1-S2).

Resilient Modulus Test Data
Summary Report
Sample: **B2-S2**

MR = 3,587.8 * B $^{0.5635}$ r = 0.97576

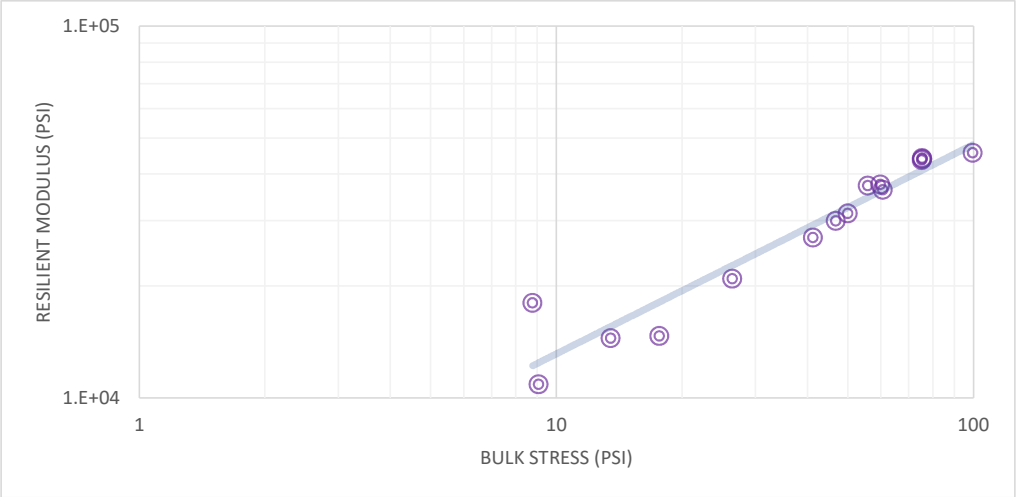

Test Date: 01/16/2023

Confining Stress, S3 (psi)	Nom. Max. Deviator Stress (psi)	Mean Deviator Stress (psi)	Std. Dev. Deviator Stress (psi)	Mean Bulk Stress (psi)	Mean Resilient Strain (%)	Std. Dev. Resilient Strain (%)	Mean Resilient Modulus (psi)	Std. Dev. Resilient Modulus (psi)
3.063	3	-0.1166	0.2767	9.071	0.00	0.00	10877	2096
2.917	6	0.02217	0.3700	8.775	0.00	0.00	18017	6241
3.006	9	4.492	3.4850	13.51	0.03	0.02	14461	1989
5.187	5	2.105	2.9577	17.67	0.02	0.02	14667	2190
5.05	10	11.28	5.6504	26.43	0.05	0.03	20927	930
5.15	15	25.84	1.0944	41.29	0.10	0.00	26976	571
10.13	10	16.46	2.1289	46.83	0.05	0.01	29912	724
10.18	20	19.49	0.9680	50.04	0.06	0.00	31358	475
10.25	30	29.93	1.3699	60.68	0.08	0.00	36277	492
15.03	10	10.75	5.4843	55.86	0.03	0.02	37239	787
15.08	15	14.61	5.4993	59.86	0.04	0.01	37493	2028
15.08	30	30.01	0.1902	75.26	0.07	0.00	43602	292
20.17	15	14.81	1.6545	75.33	0.03	0.00	44194	869
20.11	20	15.12	2.6810	75.46	0.03	0.01	43971	1764
19.96	40	39.85	6.3854	99.73	0.08	0.01	45637	1546

Figure 29. Resilient modulus test data of sample 2 of batch 2 (B2-S2).

Resilient Modulus Test Data
Summary Report
Sample: **B2-S3**

MR = 4,208.7 * B $^{0.546}$ r = 0.81695

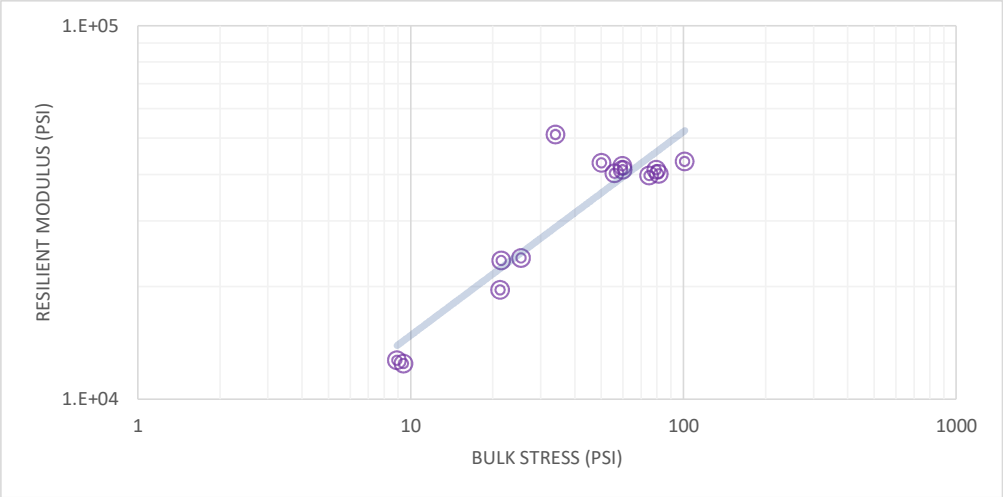

Test Date: 01/16/2023

Confining Stress, S3 (psi)	Nom. Max. Deviator Stress (psi)	Mean Deviator Stress (psi)	Std. Dev. Deviator Stress (psi)	Mean Bulk Stress (psi)	Mean Resilient Strain (%)	Std. Dev. Resilient Strain (%)	Mean Resilient Modulus (psi)	Std. Dev. Resilient Modulus (psi)
2.906	3	0.7249	1.9279	9.444	0.01	0.01	12431	1861
2.843	6	0.3934	0.6396	8.924	0.01	0.01	12681	1634
3.001	9	12.51	5.4518	21.51	0.05	0.02	23469	1482
5.154	5	-0.1459	0.0736	15.32	0.00	0.00		
5.103	10	10.15	5.8908	25.45	0.04	0.02	23855	3143
5.038	15	6.229	1.1230	21.34	0.03	0.00	19584	1556
10.04	10	3.94	5.7120	34.05	0.01	0.01	51058	3837
10.07	20	19.93	2.2177	50.14	0.05	0.01	42886	1158
10	30	29.78	5.0107	59.78	0.07	0.01	42054	494
15.12	10	14.66	3.5748	60.02	0.04	0.01	41081	2839
15.04	15	10.86	1.1663	55.97	0.03	0.00	40217	984
15.07	30	29.69	6.9572	74.89	0.07	0.02	39651	332
20.08	15	21.03	1.6224	81.28	0.05	0.00	40050	224
19.96	20	19.75	6.5312	79.63	0.05	0.02	41113	707
20.04	40	41.07	5.7469	101.2	0.09	0.01	43220	567

Figure 30. Resilient modulus test data of sample 3 of batch 2 (B2-S3).

Resilient Modulus Test Data
Summary Report
Sample: **B2-S4**

MR = 4,944.9 * B $^{0.4941}$ r = 0.92952

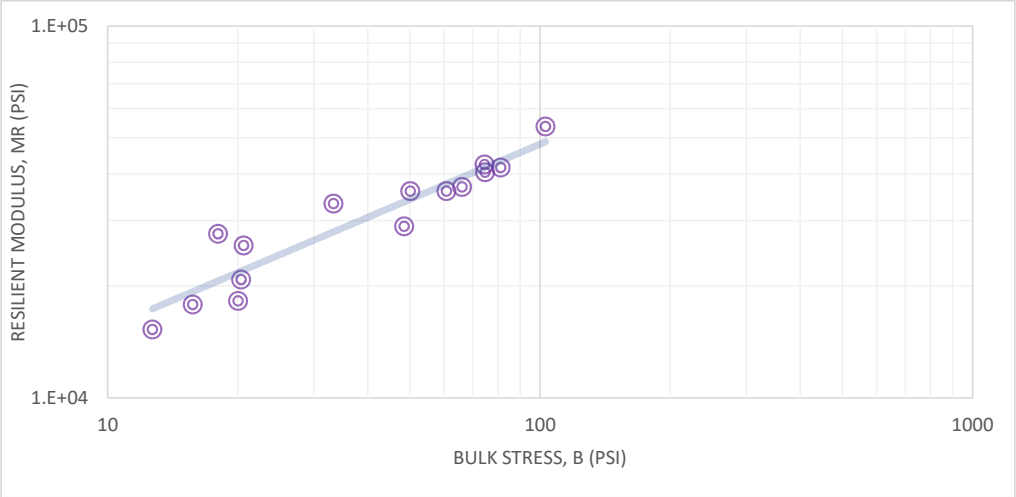

Test Date: 01/16/2023

Confining Stress, S3 (psi)	Nom. Max. Deviator Stress (psi)	Mean Deviator Stress (psi)	Std. Dev. Deviator Stress (psi)	Mean Bulk Stress (psi)	Mean Resilient Strain (%)	Std. Dev. Resilient Strain (%)	Mean Resilient Modulus (psi)	Std. Dev. Resilient Modulus (psi)
2.898	3	4.022	3.6183	12.71	0.03	0.02	15268	1042
2.956	6	6.891	6.7773	15.76	0.04	0.03	17819	2941
3.087	9	10.8	5.1251	20.06	0.06	0.02	18198	4716
5.117	5	5.043	5.0763	20.39	0.03	0.02	20772	4774
5.119	10	2.666	2.2629	18.02	0.01	0.01	27604	1520
4.898	15	5.953	0.9507	20.65	0.02	0.00	25663	794
10.16	10	2.853	0.3657	33.32	0.01	0.00	33287	1765
10.03	20	20.11	4.7252	50.19	0.06	0.01	35957	940
10.03	30	30.74	4.6641	60.82	0.08	0.01	35944	381
15.16	10	3.044	1.4971	48.54	0.01	0.00	28923	1551
14.99	15	21.17	2.1991	66.12	0.06	0.01	36883	686
15.01	30	29.45	6.9283	74.47	0.07	0.01	42355	1547
19.88	15	15.03	4.7751	74.67	0.04	0.01	40366	1174
20.15	20	20.74	7.1300	81.18	0.05	0.02	41615	2675
20.11	40	42.74	6.6283	103.1	0.08	0.01	53593	2803

Figure 31. Resilient modulus test data of sample 4 of batch 2 (B2-S4).

APPENDIX B

UNIAXIAL COMPRESSIVE STRENGTH TEST REPORTS

UNCONFINED COMPRESSION

TEST REPORT

Sample: **B0S1** Test Date: 20/01/2023

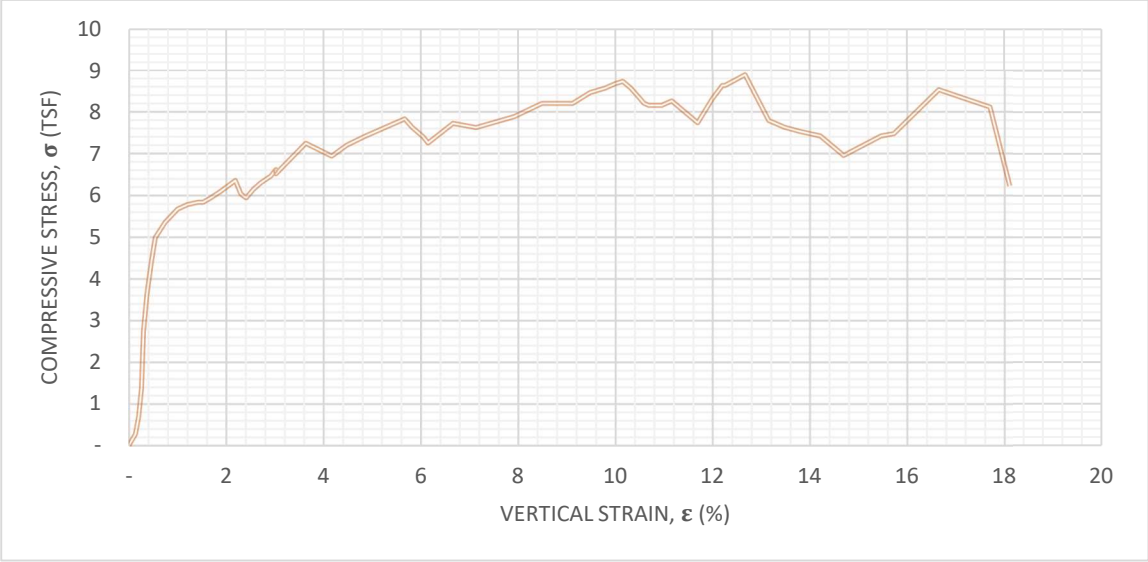

Initial	Diameter, in	2.97
	Height, in	5.67
	Water content, %	0.00
	Dry Density, pcf	23.22
	Saturation, %	0.00
	Void Ratio	6.26
Unconfined Compressive Strength, tsf		8.871
Undrained Shear Strength, tsf		4.435
Time to Failure, min		4.8825
Strain Rate, %/min		2.5
Estimated Specific Gravity		2.70

Figure 32. Unconfined compression test report of sample 1 of batch 0 (B0-S1).

UNCONFINED COMPRESSION

TEST REPORT

Sample: **B0S2** Test Date: 20/01/2023

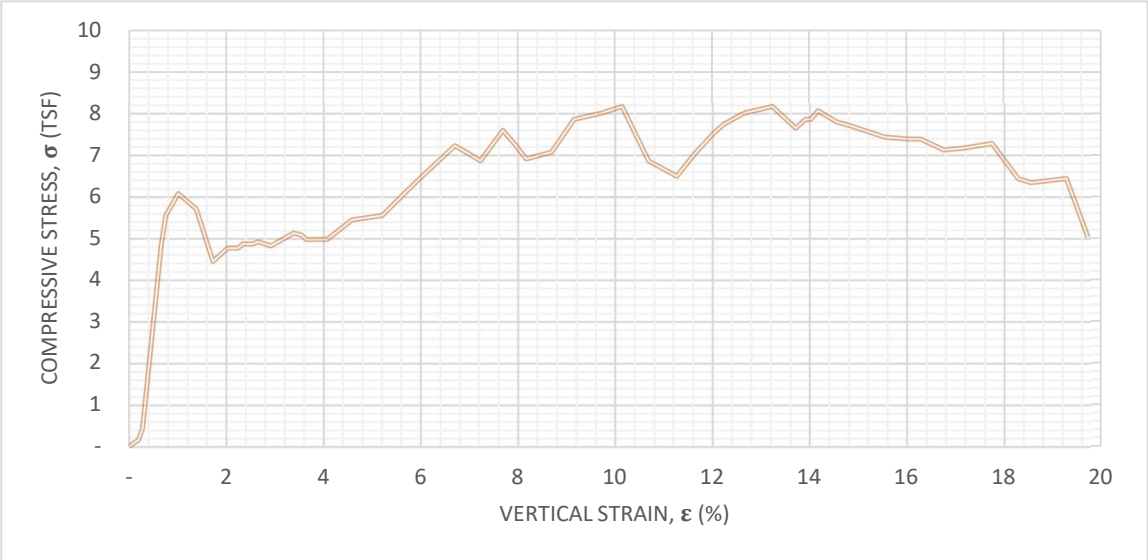

Initial	Diameter, in	2.96
	Height, in	5.67
	Water content, %	0.00
	Dry Density, pcf	23.3
	Saturation, %	0.00
	Void Ratio	6.23
Unconfined Compressive Strength, tsf		8.165
Undrained Shear Strength, tsf		4.083
Time to Failure, min		5.0644
Strain Rate, %/min		2.5
Estimated Specific Gravity		2.70

Figure 33. Unconfined compression test report of sample 2 of batch 0 (B0-S2).

UNCONFINED COMPRESSION

TEST REPORT

Sample: **B0S3** Test Date: 20/01/2023

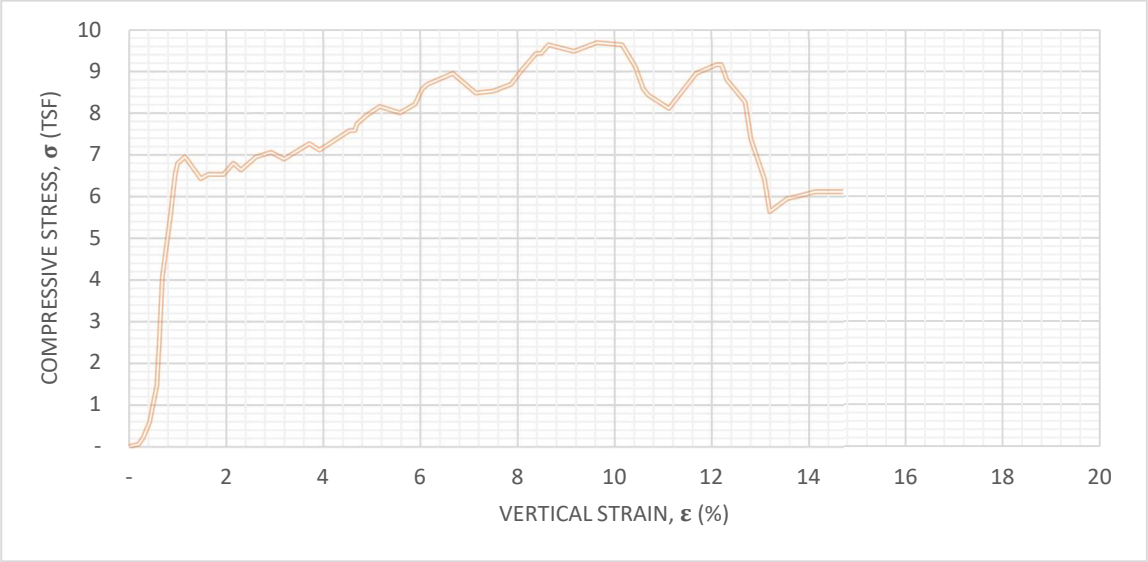

Initial	Diameter, in	2.97
	Height, in	5.73
	Water content, %	0.00
	Dry Density, pcf	23.23
	Saturation, %	0.00
	Void Ratio	6.26
Unconfined Compressive Strength, tsf		9.644
Undrained Shear Strength, tsf		4.822
Time to Failure, min		3.7502
Strain Rate, %/min		2.5
Estimated Specific Gravity		2.70

Figure 34. Unconfined compression test report of sample 3 of batch 0 (B0-S3).

UNCONFINED COMPRESSION

TEST REPORT

Sample: **B0S4** Test Date: 20/01/2023

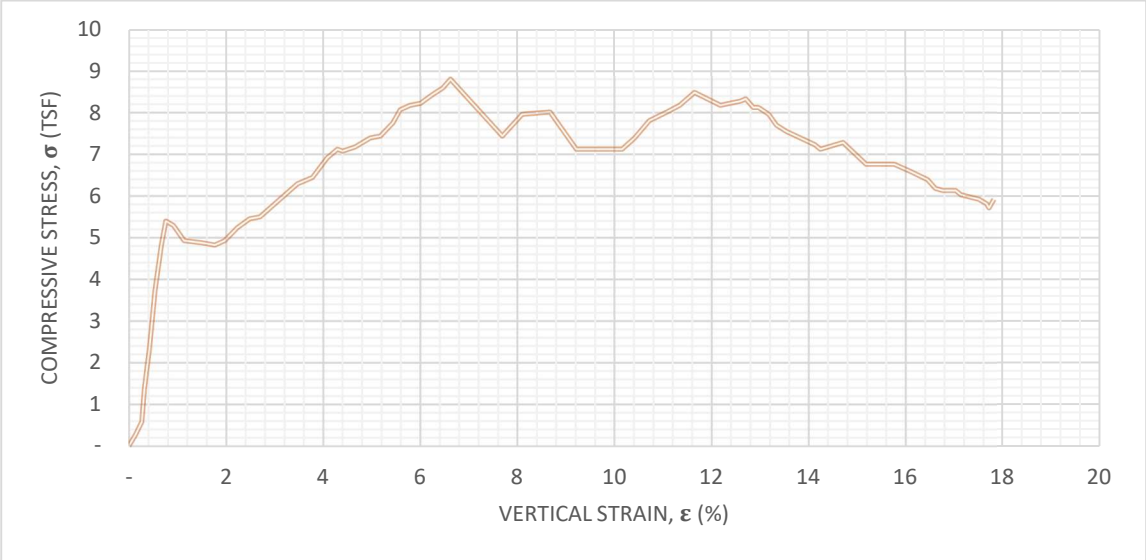

Initial	Diameter, in	2.97
	Height, in	5.65
	Water content, %	0.00
	Dry Density, pcf	23.15
	Saturation, %	0.00
	Void Ratio	6.28
Unconfined Compressive Strength, tsf		8.749
Undrained Shear Strength, tsf		4.375
Time to Failure, min		2.5814
Strain Rate, %/min		2.5
Estimated Specific Gravity		2.70

Figure 35. Unconfined compression test report of sample 4 of batch 0 (B0-S4).

UNCONFINED COMPRESSION

TEST REPORT

Sample: **B1S1** Test Date: 20/01/2023

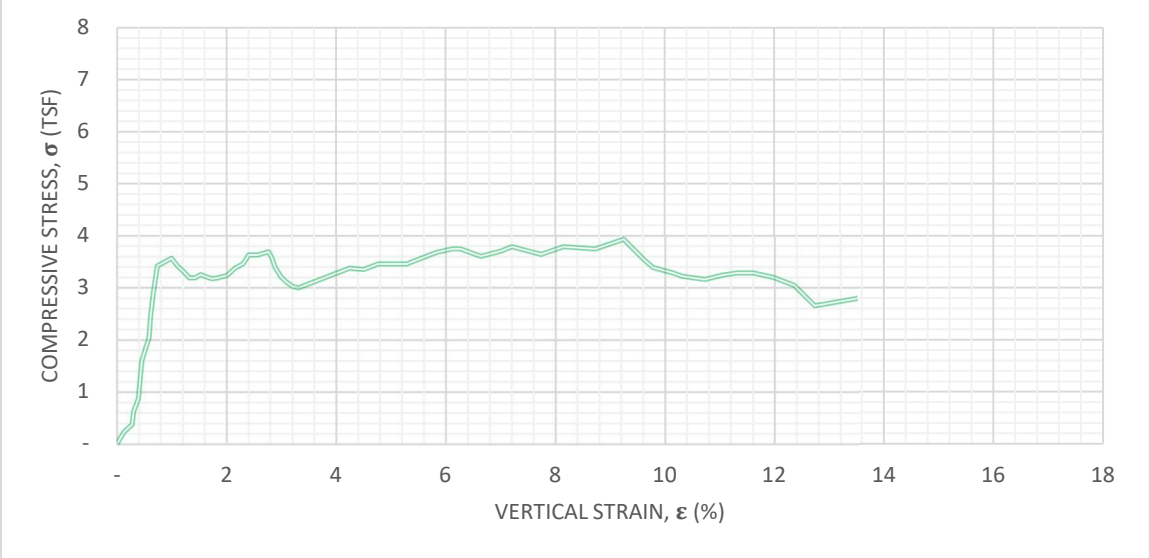

Initial	Diameter, in	3.01
	Height, in	5.27
	Water content, %	0.00
	Dry Density, pcf	19.89
	Saturation, %	0.00
	Void Ratio	7.47
Unconfined Compressive Strength, tsf		3.943
Undrained Shear Strength, tsf		1.972
Time to Failure, min		3.5872
Strain Rate, %/min		2.5
Estimated Specific Gravity		2.70

Figure 36. Unconfined compression test report of sample 1 of batch 1 (B1-S1).

UNCONFINED COMPRESSION

TEST REPORT

Sample: **B1S2** Test Date: 20/01/2023

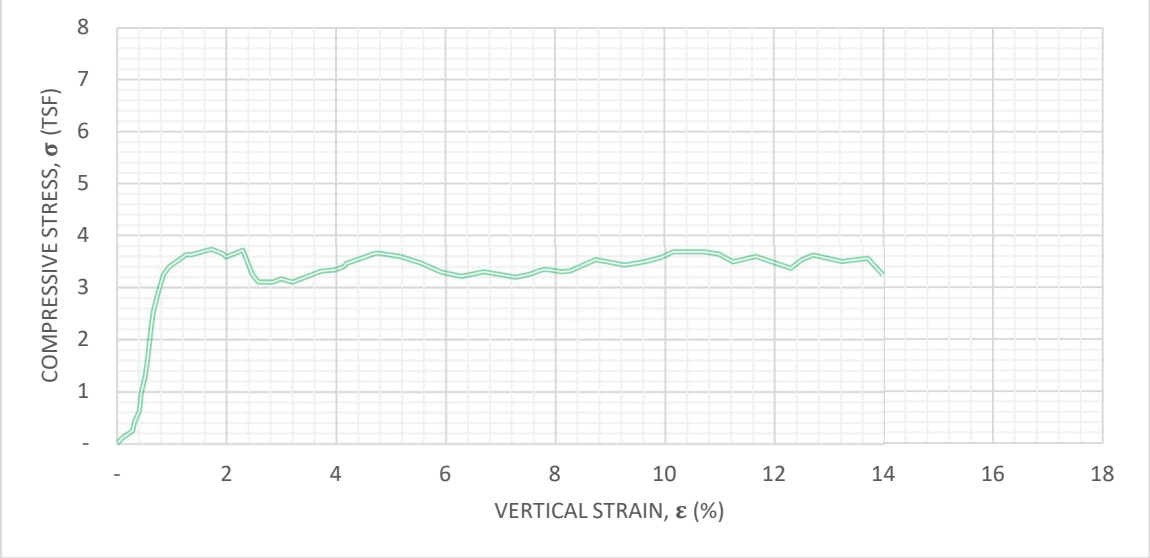

Initial	Diameter, in	3.01
	Height, in	5.33
	Water content, %	0.00
	Dry Density, pcf	19.84
	Saturation, %	0.00
	Void Ratio	7.5
Unconfined Compressive Strength, tsf		3.724
Undrained Shear Strength, tsf		1.862
Time to Failure, min		0.696
Strain Rate, %/min		2.5
Estimated Specific Gravity		2.70

Figure 37. Unconfined compression test report of sample 2 of batch 1 (B1-S2).

UNCONFINED COMPRESSION

TEST REPORT

Sample: **B1S4** Test Date: 20/01/2023

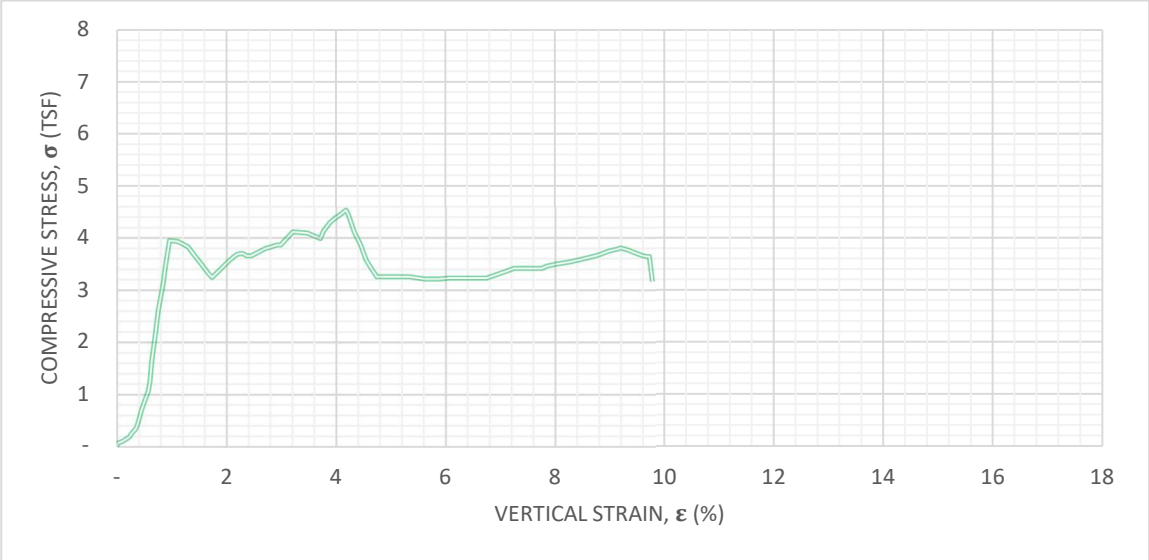

Initial	Diameter, in	3.01
	Height, in	5.01
	Water content, %	0.00
	Dry Density, pcf	19.81
	Saturation, %	0.00
	Void Ratio	7.51
Unconfined Compressive Strength, tsf		4.525
Undrained Shear Strength, tsf		2.263
Time to Failure, min		1.6422
Strain Rate, %/min		2.5
Estimated Specific Gravity		2.70

Figure 38. Unconfined compression test report of sample 4 of batch 1 (B1-S4).

UNCONFINED COMPRESSION

TEST REPORT

Sample: **B1S7** Test Date: 20/01/2023

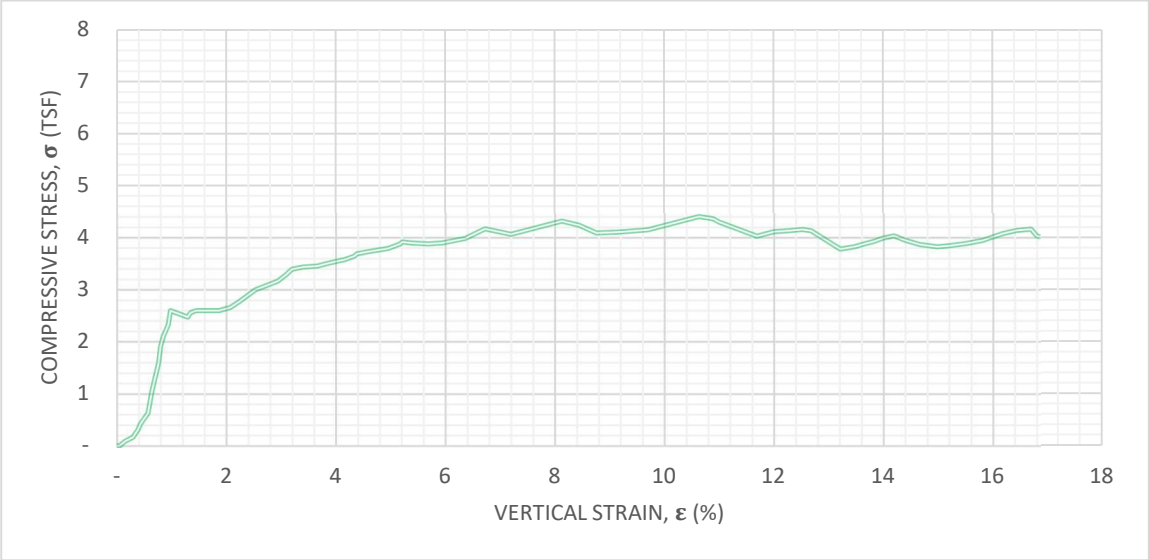

Initial	Diameter, in	3.01
	Height, in	5.25
	Water content, %	0.00
	Dry Density, pcf	20.78
	Saturation, %	0.00
	Void Ratio	7.11
Unconfined Compressive Strength, tsf		4.399
Undrained Shear Strength, tsf		2.199
Time to Failure, min		4.1573
Strain Rate, %/min		2.5
Estimated Specific Gravity		2.70

Figure 39. Unconfined compression test report of sample 7 of batch 1 (B1-S7).

UNCONFINED COMPRESSION

TEST REPORT

Sample: **B2S1** Test Date: 20/01/2023

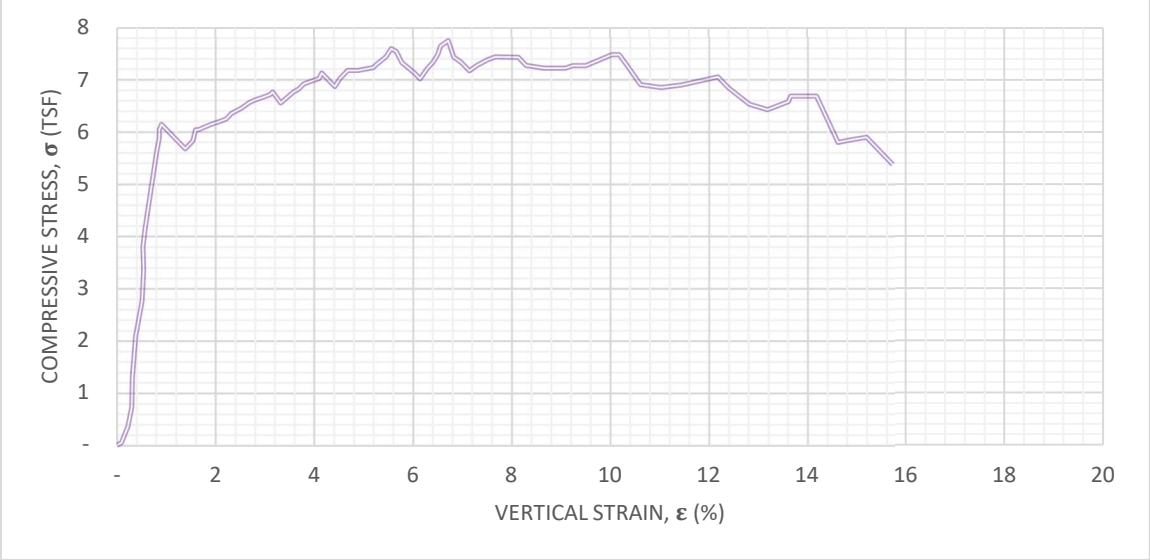

Initial	Diameter, in	3.01
	Height, in	5.03
	Water content, %	0.00
	Dry Density, pcf	21.35
	Saturation, %	0.00
	Void Ratio	6.59
Unconfined Compressive Strength, tsf		7.718
Undrained Shear Strength, tsf		3.859
Time to Failure, min		2.5996
Strain Rate, %/min		2.5
Estimated Specific Gravity		2.70

Figure 40. Unconfined compression test report of sample 1 of batch 2 (B2-S1).

UNCONFINED COMPRESSION

TEST REPORT

Sample: **B2S2** Test Date: 20/01/2023

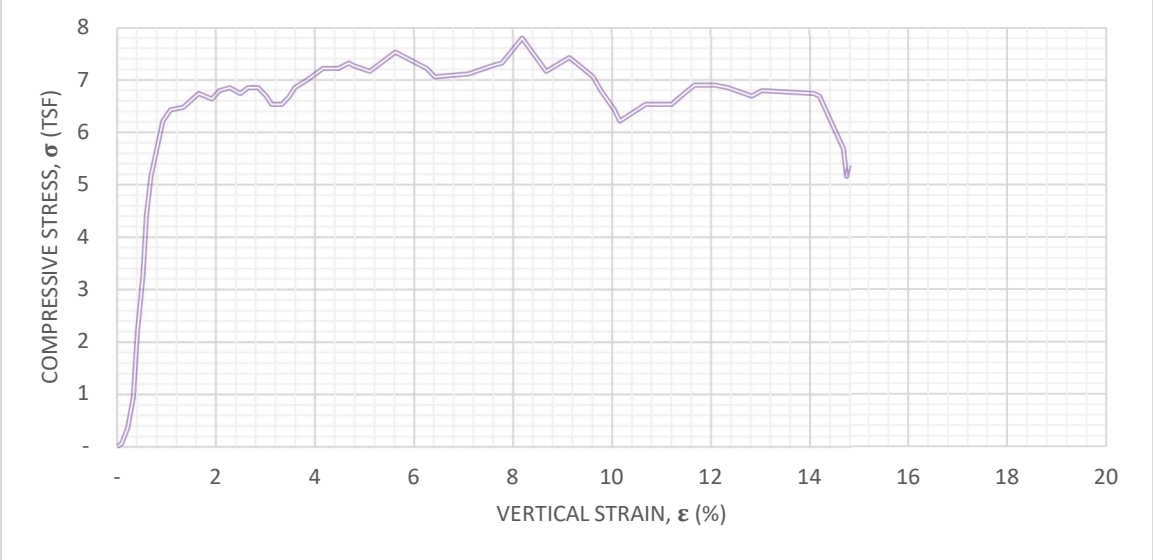

Initial	Diameter, in	3.01
	Height, in	5.08
	Water content, %	0.00
	Dry Density, pcf	20.91
	Saturation, %	0.00
	Void Ratio	7.06
Unconfined Compressive Strength, tsf		7.72
Undrained Shear Strength, tsf		3.86
Time to Failure, min		3.1671
Strain Rate, %/min		2.5
Estimated Specific Gravity		2.70

Figure 41. Unconfined compression test report of sample 2 of batch 2 (B2-S2).

UNCONFINED COMPRESSION

TEST REPORT

Sample: **B2S3** Test Date: 20/01/2023

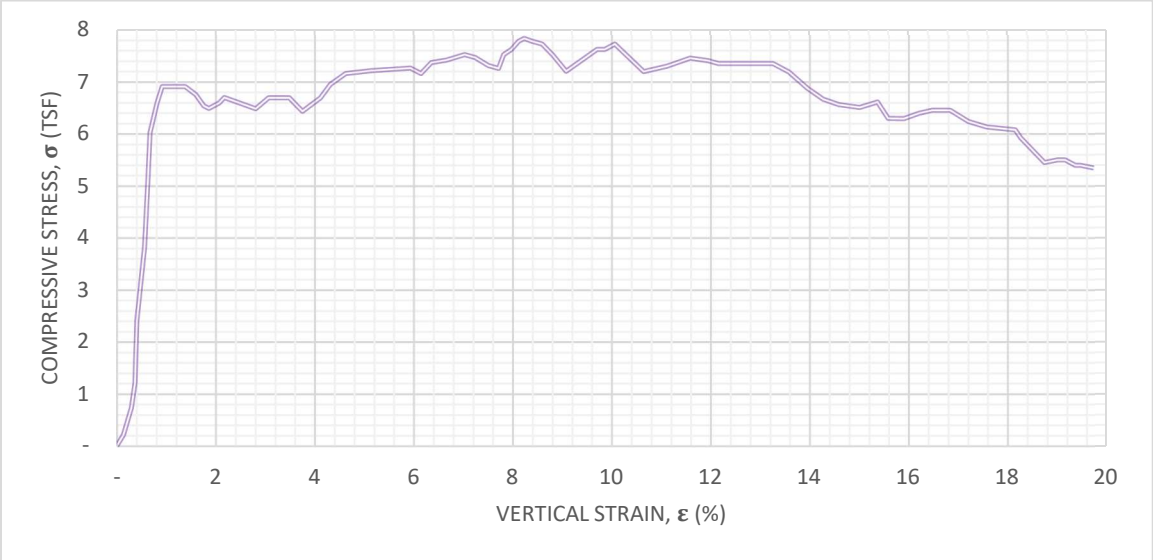

Initial	Diameter, in	3
	Height, in	5.06
	Water content, %	0.00
	Dry Density, pcf	21.16
	Saturation, %	0.00
	Void Ratio	6.97
Unconfined Compressive Strength, tsf		7.861
Undrained Shear Strength, tsf		3.93
Time to Failure, min		3.1705
Strain Rate, %/min		2.5
Estimated Specific Gravity		2.70

Figure 42. Unconfined compression test report of sample 3 of batch 2 (B2-S3).

UNCONFINED COMPRESSION

TEST REPORT

Sample: **B2S4** Test Date: 20/01/2023

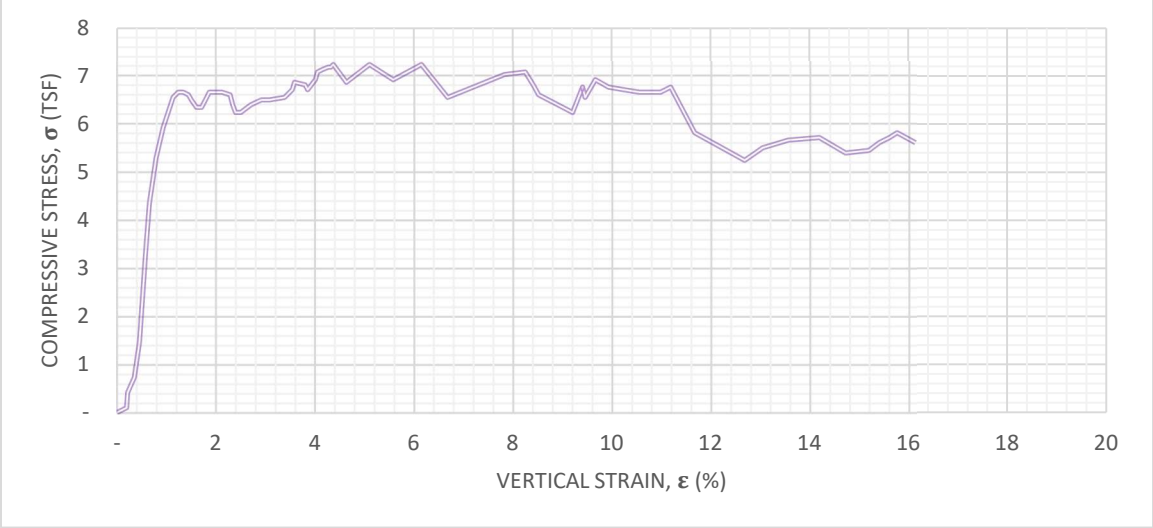

Initial	Diameter, in	3.01
	Height, in	5.15
	Water content, %	0.00
	Dry Density, pcf	21.14
	Saturation, %	0.00
	Void Ratio	6.97
Unconfined Compressive Strength, tsf		7.268
Undrained Shear Strength, tsf		3.634
Time to Failure, min		1.7248
Strain Rate, %/min		2.5
Estimated Specific Gravity		2.70

Figure 43. Unconfined compression test report of sample 4 of batch 2 (B2-S4).

APPENDIX C

GRAPH'S SCALE TRANSFORMATION

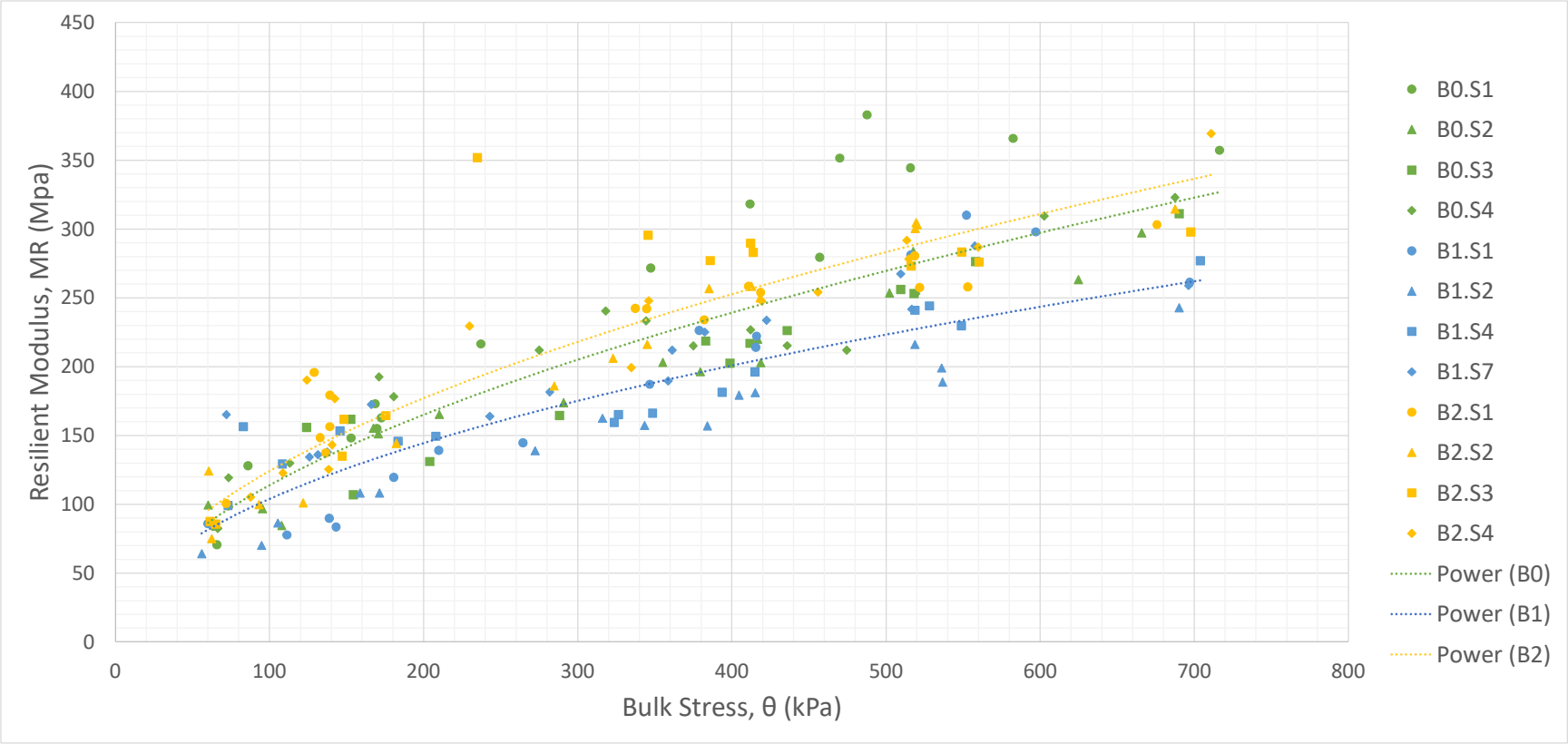

Figure 44. Graphical Results of the resilient modulus tests at a regular scale.

Table 13. Batch's 0 data.

Batch	Sample	Mean Bulk Stress, θ (kPa)	Mean Resilient Modulus, MR (mPa)	log(θ)	log(MR)
B 0	S 1	65.838	70.635	1.818	1.849
		86.047	128.028	1.935	2.107
		168.508	173.023	2.227	2.238
		172.507	162.723	2.237	2.211
		169.680	155.127	2.230	2.191
		152.926	148.101	2.184	2.171
		237.111	216.533	2.375	2.336
		347.289	271.605	2.541	2.434
		411.755	318.212	2.615	2.503
		456.985	279.341	2.660	2.446
		470.016	351.506	2.672	2.546
		515.797	344.402	2.712	2.537
		487.666	382.884	2.688	2.583
		582.469	365.765	2.765	2.563
		716.365	357.201	2.855	2.553
	S 2	60.164	99.416	1.779	1.997
		95.354	96.708	1.979	1.985
		167.474	155.275	2.224	2.191
		107.972	84.468	2.033	1.927
		170.507	151.208	2.232	2.180
		210.083	165.162	2.322	2.218
		290.821	173.713	2.464	2.240
		355.149	203.159	2.550	2.308
		416.788	219.898	2.620	2.342
		379.556	196.193	2.579	2.293
		418.788	202.664	2.622	2.307
		502.283	253.378	2.701	2.404
		517.589	283.699	2.714	2.453
		624.872	263.144	2.796	2.420
		665.965	297.178	2.823	2.473
	S 3	65.066	84.093	1.813	1.925
		154.374	106.926	2.189	2.029
		124.106	155.761	2.094	2.192
		152.788	161.813	2.184	2.209
		203.878	131.005	2.309	2.117
		288.201	164.597	2.460	2.216
		398.724	202.384	2.601	2.306
		411.755	216.912	2.615	2.336
		383.004	218.547	2.583	2.340
		435.749	226.241	2.639	2.355
		518.210	253.066	2.715	2.403
		509.523	256.052	2.707	2.408
		558.200	276.279	2.747	2.441
		690.165	311.101	2.839	2.493
		66.348	82.417	1.822	1.916
	S 4	73.429	119.244	1.866	2.076
		180.643	178.172	2.257	2.251
		113.212	129.869	2.054	2.114
		171.059	192.629	2.233	2.285
		274.963	211.928	2.439	2.326
		318.055	240.417	2.503	2.381
		344.255	233.261	2.537	2.368
		412.100	226.760	2.615	2.356
		374.868	215.129	2.574	2.333
		435.956	215.275	2.639	2.333
		519.313	253.202	2.715	2.403
		474.497	211.863	2.676	2.326
		602.533	309.408	2.780	2.491
		687.476	322.905	2.837	2.509
Equation in	power format	$MR = 9.6674\theta^{0.5355}$			
	linear format	$\log(MR) = 0.5355*\log(\theta) + 0.9853$			

Table 14. Batch's 0 data regression summary output.

Regular Scale

Regression Statistics	
Multiple R	0.88924386
R Square	0.790754643
Adjusted R Square	0.787083671
Standard Error	36.2052559
Observations	59

ANOVA

	df	*SS*	*MS*	*F*	*Significance F*
Regression	1	282360.5492	282360.5492	215.4074776	5.12674E-21
Residual	57	74716.77161	1310.820555		
Total	58	357077.3208			

	Coefficients	*Standard Error*	*t Stat*	*P-value*	*Lower 95%*	*Upper 95%*	*Lower 95.0%*	*Upper 95.0%*
Intercept	86.3231	9.7438	8.8593	0.0000	66.8114	105.8348	66.8114	105.8348
X Variable 1	0.3698	0.0252	14.6768	0.0000	0.3194	0.4203	0.3194	0.4203

Logarithmic Scale

Regression Statistics	
Multiple R	0.921837215
R Square	0.84978385
Adjusted R Square	0.847148479
Standard Error	0.069622125
Observations	59

ANOVA

	df	*SS*	*MS*	*F*	*Significance F*
Regression	1	1.5630	1.5630	322.4532	0.0000
Residual	57	0.2763	0.0048		
Total	58	1.8393			

	Coefficients	*Standard Error*	*t Stat*	*P-value*	*Lower 95%*	*Upper 95%*	*Lower 95.0%*	*Upper 95.0%*
Intercept	0.9853	0.0733	13.4340	0.0000	0.8384	1.1322	0.8384	1.1322
X Variable 1	0.5355	0.0298	17.9570	0.0000	0.4758	0.5952	0.4758	0.5952

Table 15. Batch's 1 data.

Batch	Sample	Mean Bulk Stress, θ (kPa)	Mean Resilient Modulus, MR (mPa)	log(θ)	log(MR)
B 1	S 1	59.998	85.850	1.778	1.934
		143.204	83.523	2.156	1.922
		138.723	89.825	2.142	1.953
		111.350	77.755	2.047	1.891
		180.574	119.502	2.257	2.077
		209.807	139.126	2.322	2.143
		264.345	144.635	2.422	2.160
		346.668	187.112	2.540	2.272
		415.961	222.153	2.619	2.347
		378.798	226.352	2.578	2.355
		415.478	214.003	2.619	2.330
		516.142	281.166	2.713	2.449
		597.086	297.940	2.776	2.474
		552.201	310.031	2.742	2.491
		697.060	261.295	2.843	2.417
	S 2	55.972	64.113	1.748	1.807
		105.490	86.323	2.023	1.936
		94.872	70.051	1.977	1.845
		158.717	108.125	2.201	2.034
		171.335	108.160	2.234	2.034
		272.343	138.853	2.435	2.143
		316.056	162.512	2.500	2.211
		343.359	157.146	2.536	2.196
		415.133	181.026	2.618	2.258
		384.107	156.913	2.584	2.196
		404.653	179.188	2.607	2.253
		518.762	216.002	2.715	2.334
		536.067	198.997	2.729	2.299
		536.688	188.764	2.730	2.276
		690.165	242.750	2.839	2.385
	S 4	73.084	99.122	1.864	1.996
		83.082	156.307	1.920	2.194
		145.686	153.213	2.163	2.185
		108.317	129.213	2.035	2.111
		207.877	149.367	2.318	2.174
		183.332	145.831	2.263	2.164
		326.329	165.115	2.514	2.218
		348.599	166.132	2.542	2.220
		414.926	196.027	2.618	2.292
		323.640	159.433	2.510	2.203
		393.553	181.371	2.595	2.259
		518.693	240.892	2.715	2.382
		528.207	244.121	2.723	2.388
		548.961	229.726	2.740	2.361
		703.955	276.842	2.848	2.442
	S 7	71.912	165.031	1.857	2.218
		137.413	137.895	2.138	2.140
		125.898	134.201	2.100	2.128
		166.095	172.415	2.220	2.237
		131.414	136.072	2.119	2.134
		242.902	163.868	2.385	2.214
		281.789	181.516	2.450	2.259
		358.665	189.468	2.555	2.278
		422.511	233.727	2.626	2.369
		382.383	225.091	2.582	2.352
		361.216	211.930	2.558	2.326
		516.693	241.715	2.713	2.383
		509.523	267.285	2.707	2.427
		557.648	287.717	2.746	2.459
Equation in	power format	$MR = 11.636\theta^{0.4754}$			
	linear format	$\log(MR) = 0.4757*\log(\theta) + 1.0651$			

Table 16. Batch's 1 data regression summary output.

Regular Scale

Regression Statistics	
Multiple R	0.778505509
R Square	0.606070828
Adjusted R Square	0.59915979
Standard Error	38.77990478
Observations	59

ANOVA

	df	*SS*	*MS*	*F*	*Significance F*
Regression	1	131884.4429	131884.4429	87.69606214	3.94085E-13
Residual	57	85721.21783	1503.881015		
Total	58	217605.6607			

	Coefficients	*Standard Error*	*t Stat*	*P-value*	*Lower 95%*	*Upper 95%*	*Lower 95.0%*	*Upper 95.0%*
Intercept	91.4068	10.4367	8.7582	0.0000	70.5076	112.3060	70.5076	112.3060
X Variable 1	0.2528	0.0270	9.3646	0.0000	0.1987	0.3068	0.1987	0.3068

Logarithmic Scale

Regression Statistics	
Multiple R	0.747823367
R Square	0.559239789
Adjusted R Square	0.551507153
Standard Error	0.11066214
Observations	59

ANOVA

	df	*SS*	*MS*	*F*	*Significance F*
Regression	1	0.885663334	0.885663334	72.32201803	1.00564E-11
Residual	57	0.698028227	0.012246109		
Total	58	1.583691562			

	Coefficients	*Standard Error*	*t Stat*	*P-value*	*Lower 95%*	*Upper 95%*	*Lower 95.0%*	*Upper 95.0%*
Intercept	1.2354	0.1166	10.5974	0.0000	1.0020	1.4689	1.0020	1.4689
X Variable 1	0.4031	0.0474	8.5042	0.0000	0.3082	0.4980	0.3082	0.4980

Table 17. Batch's 2 data.

Batch	Sample	Mean Bulk Stress, θ (kPa)	Mean Resilient Modulus, MR (mPa)	log(θ)	log(MR)
B 2	S 1	71.843	100.605	1.856	2.003
		132.793	148.364	2.123	2.171
		138.998	156.284	2.143	2.194
		129.001	195.809	2.111	2.292
		139.136	179.204	2.143	2.253
		136.447	137.286	2.135	2.138
		337.292	242.276	2.528	2.384
		344.669	242.033	2.537	2.384
		418.581	253.803	2.622	2.404
		381.970	233.957	2.582	2.369
		410.721	258.250	2.614	2.412
		518.555	280.540	2.715	2.448
		521.864	257.521	2.718	2.411
		553.028	257.883	2.743	2.411
		675.824	303.150	2.830	2.482
	S 2	62.542	74.939	1.796	1.875
		60.501	124.141	1.782	2.094
		93.148	99.633	1.969	1.998
		121.830	101.054	2.086	2.005
		182.228	144.190	2.261	2.159
		284.685	185.862	2.454	2.269
		322.881	206.091	2.509	2.314
		345.014	216.055	2.538	2.335
		418.374	249.946	2.622	2.398
		385.141	256.575	2.586	2.409
		412.720	258.330	2.616	2.412
		518.899	300.421	2.715	2.478
		519.382	304.495	2.715	2.484
		520.278	302.957	2.716	2.481
		687.614	314.438	2.837	2.498
	S 3	65.114	85.646	1.814	1.933
		61.529	87.373	1.789	1.941
		148.306	161.704	2.171	2.209
		175.472	164.361	2.244	2.216
		147.134	134.931	2.168	2.130
		234.766	351.791	2.371	2.546
		345.703	295.485	2.539	2.471
		412.169	289.752	2.615	2.462
		413.823	283.048	2.617	2.452
		385.900	277.092	2.586	2.443
		516.348	273.194	2.713	2.436
		560.406	275.942	2.749	2.441
		549.030	283.269	2.740	2.452
		697.749	297.784	2.844	2.474
	S 4	87.632	105.195	1.943	2.022
		108.661	122.770	2.036	2.089
		138.309	125.381	2.141	2.098
		140.584	143.121	2.148	2.156
		124.244	190.193	2.094	2.279
		142.377	176.821	2.153	2.248
		229.733	229.350	2.361	2.360
		346.048	247.744	2.539	2.394
		419.339	247.651	2.623	2.394
		334.672	199.282	2.525	2.299
		455.881	254.125	2.659	2.405
		513.453	291.827	2.711	2.465
		514.832	278.122	2.712	2.444
		559.716	286.727	2.748	2.457
Equation in	power format	$MR = 11.715\theta^{0.5125}$			
	linear format	$\log(MR) = 0.5097*\log(\theta) + 1.075$			

Table 18. Batch's 2 data regression summary output.

Regular Scale

Regression Statistics	
Multiple R	0.88924386
R Square	0.790754643
Adjusted R Square	0.787083671
Standard Error	36.2052559
Observations	59

ANOVA

	df	*SS*	*MS*	*F*	*Significance F*
Regression	1	282360.5492	282360.5492	215.4074776	5.12674E-21
Residual	57	74716.77161	1310.820555		
Total	58	357077.3208			

	Coefficients	*Standard Error*	*t Stat*	*P-value*	*Lower 95%*	*Upper 95%*	*Lower 95.0%*	*Upper 95.0%*
Intercept	86.3231	9.7438	8.8593	0.0000	66.8114	105.8348	66.8114	105.8348
X Variable 1	0.3698	0.0252	14.6768	0.0000	0.3194	0.4203	0.3194	0.4203

Logarithmic Scale

Regression Statistics	
Multiple R	0.921837215
R Square	0.84978385
Adjusted R Square	0.847148479
Standard Error	0.069622125
Observations	59

ANOVA

	df	*SS*	*MS*	*F*	*Significance F*
Regression	1	1.5630	1.5630	322.4532	0.0000
Residual	57	0.2763	0.0048		
Total	58	1.8393			

	Coefficients	*Standard Error*	*t Stat*	*P-value*	*Lower 95%*	*Upper 95%*	*Lower 95.0%*	*Upper 95.0%*
Intercept	0.9853	0.0733	13.4340	0.0000	0.8384	1.1322	0.8384	1.1322
X Variable 1	0.5355	0.0298	17.9570	0.0000	0.4758	0.5952	0.4758	0.5952

REFERENCES

[1] A. Fini, P. Frangi, J. Mori, D. Donzelli, and F. Ferrini, "Nature based solutions to mitigate soil sealing in urban areas: Results from a 4-year study comparing permeable, porous, and impermeable pavements," *Environmental Research,* vol. 156, pp. 443-454, 2017.

[2] J. R. Warhurst, K. E. Parks, L. McCulloch, and M. D. Hudson, "Front gardens to car parks: changes in garden permeability and effects on flood regulation," *Science of the Total Environment,* vol. 485, pp. 329-339, 2014.

[3] B. Shackel, "Design of permeable paving subject to traffic," in *8th International Conference on Concrete Block Paving*, 2006, pp. 6-8.

[4] X. Guan, J. Wang, and F. Xiao, "Sponge city strategy and application of pavement materials in sponge city," *Journal of Cleaner Production,* vol. 303, p. 127022, 2021.

[5] A. Kia, H. S. Wong, and C. R. Cheeseman, "Clogging in permeable concrete: A review," *Journal of Environmental Management,* vol. 193, pp. 221-233, 2017.

[6] N. Su, F. Xiao, J. Wang, and S. Amirkhanian, "Characterizations of base and subbase layers for Mechanistic-Empirical Pavement Design," *Construction and Building Materials,* vol. 152, pp. 731-745, 2017.

[7] P. Kumar, S. Chandra, and R. Vishal, "Comparative study of different subbase materials," *Journal of Materials in Civil Engineering,* vol. 18, no. 4, pp. 576-580, 2006.

[8] N. Sutmoller, M. Gomez, and J. T. Kevern, "Soft soil remediation with permeable low-density cellular concrete," *IFCEE 2021,* pp. 196-202.

[9] N. Sutmoller and M. Gomez, "An introduction to low-density cellular concrete and advanced engineered foam technology," *North American Tunneling 2022 Proceedings,* 2022.

[10] E. National Academies of Sciences and Medicine, *Framing the Challenge of Urban Flooding in the United States*. National Academies Press, 2019.

[11] V. Masson-Delmotte, P. Zhai, H.-O. Pörtner, D. Roberts, J. Skea, and P. R. Shukla, *Global Warming of 1.5° C: IPCC Special Report on Impacts of Global Warming of 1.5° C above Pre-industrial Levels in Context of Strengthening Response to Climate Change, Sustainable Development, and Efforts to Eradicate Poverty*. Cambridge University Press, 2022.

[12] J. Xia, Y. Zhang, L. Xiong, S. He, L. Wang, and Z. Yu, "Opportunities and challenges of the Sponge City construction related to urban water issues in China," *Science China Earth Sciences,* vol. 60, no. 4, pp. 652-658, 2017.

[13] C. Song, "Application of nature-based measures in China's sponge city initiative: Current trends and perspectives," *Nature-Based Solutions,* vol. 2, p. 100010, 2022.

[14] J. Wang *et al.*, "Regenerating sponge city to sponge watershed through an innovative framework for urban water resilience," *Sustainability,* vol. 13, no. 10, p. 5358, 2021. [Online]. Available: https://www.mdpi.com/2071-1050/13/10/5358.

[15] T. T. Nguyen *et al.*, "Implementation of a specific urban water management-Sponge City," *Science of the Total Environment,* vol. 652, pp. 147-162, 2019.

[16] M. D. Allen, J. Argue, W. Geiger, L. Johnston, D. Pezzaniti, and P. Scott, "Water sensitive urban design: Basic procedures for source control of stormwater: a handbook for Australian practice," University of South Australia, 2004, p. 246.

[17] Y. Mai, M. Zhang, W. Chen, X. Chen, G. Huang, and D. Li, "Experimental study on the effects of LID measures on the control of rainfall runoff," *Urban Water Journal,* vol. 15, no. 9, pp. 827-836, 2018.

[18] V. R. Schaefer, J. T. Kevern, B. Izevbekhai, K. Wang, H. E. Cutler, and P. Wiegand, "Construction and performance of pervious concrete overlay at minnesota road research project," *Transportation Research Record,* vol. 2164, no. 1, pp. 82-88, 2010.

[19] R. B. Mallick and T. El-Korchi, *Pavement Engineering: Principles and Practice*. CRC Press, 2008.

[20] D. V. Muttuvelu and E. Kjems, "A systematic review of permeable pavements and their unbound material properties in comparison to traditional subbase Materials," *Infrastructures,* vol. 6, no. 12, p. 179, 2021.

[21] P. T. Weiss, M. Kayhanian, J. S. Gulliver, and L. Khazanovich, "Permeable pavement in northern North American urban areas: research review and knowledge gaps," *International Journal of Pavement Engineering,* vol. 20, no. 2, pp. 143-162, 2019.

[22] A. Ralla, S. Saadeh, J. Harvey, and E. Mahmoud, "Sustainable mitigation of stormwater runoff through fully permeable pavement," in *Advances in Materials and Pavement Performance Prediction*: CRC Press, 2018, pp. 327-330.

[23] Y. M. Amran, N. Farzadnia, and A. A. Ali, "Properties and applications of foamed concrete; a review," *Construction and Building Materials,* vol. 101, pp. 990-1005, 2015.

[24] B. Tiwari, B. Ajmera, R. Maw, R. Cole, D. Villegas, and P. Palmerson, "Mechanical properties of lightweight cellular concrete for geotechnical applications," *Journal of Materials in Civil Engineering,* vol. 29, no. 7, p. 06017007, 2017.

[25] S. Taylor and G. Halsted, "Guide to lightweight cellular concrete for geotechnical applications," *PCA Special Rep. No. SR1008P. Washington, DC: Portland Cement Association,* 2021.

[26] A. Raj, D. Sathyan, and K. Mini, "Physical and functional characteristics of foam concrete: A review," *Construction and Building Materials,* vol. 221, pp. 787-799, 2019.

[27] A. C. 523 and A. C. Institute, *ACI 523. 3R-14 Guide for Cellular Concretes Above 50 Lb/ft3 (800 Kg/m3)*. American Concrete Institute, 2014.

[28] L. Chica and A. Alzate, "Cellular concrete review: New trends for application in construction," *Construction and Building Materials,* vol. 200, pp. 637-647, 2019.

[29] E. Kearsley and P. Wainwright, "Porosity and permeability of foamed concrete," *Cement and Concrete Research,* vol. 31, no. 5, pp. 805-812, 2001.

[30] N. M. Zahari, I. A. Rahman, A. M. A. Zaidi, and A. Mujahid, "Foamed concrete: Potential application in thermal insulation," in *Malaysian Technical Universities Conference on Engineering and Technology*, 2009, pp. 47-52.

[31] J. Eskew, K. Hill, L. Madrid, N. Sutmoller, and L. C. Updike Jr, "Soft soil settlement remediation and roadway elevation increase with Permeable Low-Density Cellular Concrete (PLDCC)," in *Geo-Extreme 2021*, 2021, pp. 90-100.

[32] S. Inti, T. W. Evans III, M. Flores, J. S. Solanki, and C. V. Chandramouli, "Permeable low-density cellular concrete (PLDCC) as a replacement for aggregate layers in permeable parking lots," *Developments in the Built Environment,* vol. 8, p. 100060, 2021.

[33] T. Bennert and A. Maher, "The development of a performance specification for granular base and subbase material," New Jersey. Dept. of Transportation, 2005.

[34] J. T. Kevern, "Basic characterization of permeable cellular concrete," Unpublished confidential document, 2018.